Architecture of the MKK6-p38α complex defines the basis of MAPK specificity and activation

Pauline Juyoux[1], Ioannis Galdadas[2, 3†], Dorothea Gobbo[2, 3†], Mark Tully[4], Francesco Luigi Gervasio[2,3,5,6], Erika Pellegrini[1]* and Matthew W. Bowler[1]*

Affiliations:

[1] European Molecular Biology Laboratory; Grenoble, France.

[2] Institute of Pharmaceutical Sciences of Western Switzerland, University of Geneva; Geneva, Switzerland

[3] School of Pharmaceutical Sciences, University of Geneva; Geneva, Switzerland.

[4] European Synchrotron Radiation Facility; Grenoble, France.

[5] Department of Chemistry, University College London; London, UK

[6] Institute of Structural and Molecular Biology, University College London; London, UK

*Corresponding authors. Email: epellegr@embl.fr, mbowler@embl.fr

†These authors contributed equally

Abstract

The MAP kinase p38α is a central component of signalling in inflammation and the immune response, and is therefore an important drug target. Little is known about the molecular mechanism of its activation by double-phosphorylation from MAP2Ks, due to the challenge of trapping a transient and dynamic hetero-kinase complex. Here, we applied a multidisciplinary approach to generate the first structure of p38α in complex with its MAP2K MKK6 and understand the activation mechanism. Integrating cryo-EM with MD simulations and *in cellulo* experiments, we demonstrate a dynamic, multi-step, phosphorylation mechanism, reveal new catalytically relevant interactions, and show that MAP2K disordered N-termini determine pathway specificity. Our work captures, for the first time, a fundamental step of cell signalling: a kinase phosphorylating its downstream target kinase.

One-Sentence Summary: Integrative Cryo-EM and MD analysis of an active hetero-kinase complex reveals details of cellular signal transmission

Main Text: The mitogen activated protein kinases (MAPKs) are conserved in all eukaryotes where they form signalling cascades responding to extra-cellular stimuli leading to diverse responses from differentiation to apoptosis. In higher organisms, the MAPK p38α acts in response to stress such as irradiation, hypoxia and osmotic shock, and also to signalling from inflammatory cytokines (*1*). Pathogens often elicit upregulation of p38α, with particular relevance in the current pandemic, where SARS-CoV-2 has been shown to promote p38α activation leading to the cytokine storm responsible for the Chronic Obstructive Pulmonary Disease (COPD) associated with severe COVID19 (*2*, *3*). Signals propagate through phosphorylation of successive protein kinases (MAP4K, MAP3K to MAP2K), which eventually phosphorylate and activate a MAPK via double phosphorylation at the TxY motif in the activation loop (A-loop), leading to a conformational change (*4*, *5*). When the A-loop is phosphorylated, key residues surrounding the ATP and Mg^{2+} ions reorient, stabilising the activated MAPK. The activated MAPK is then transported to the nucleus where it modulates gene expression (*6*-*8*). The key role of p38α in inflammation, and the fact that aberrant p38α signalling is implicated in numerous diseases, such as arthritis and cancer, but also in the response to infection, makes it a highly studied drug target (*1*). Despite initial successes in developing potent compounds targeting the kinase nucleotide binding pocket, many potential therapies failed in clinical trials due to off target effects (*9*). Therefore, a molecular understanding of its interaction with upstream activators is essential in order to develop new strategies to target either p38, or its activators. The structures of individual MAPKs (*10*-*12*) and MAP2Ks (*13*-*16*) have been extensively studied and subsequent work has defined the interacting regions between these partners (*17*-*20*). The MAP2Ks contain a kinase interaction motif (KIM) at the start of their intrinsically disordered N-termini, which interacts with an allosteric docking site on their target MAPK. The KIM partially ensures specificity between members of the

pathway (*17*), acts allosterically to expose the A-loop, preparing the MAPK for activation (*21*, *22*), and also enhances the local concentration of kinase and substrate (*23*). However, there is little structural data on the global interactions between MAP kinase cascade components. In particular, beyond the KIM interaction, molecular details of selectivity and activation of a MAPK by its upstream MAP2K remain unknown. Moreover, our knowledge of kinase-kinase interactions in general is restricted to homo-dimers and inactive conformations (*24-27*).

In order to further our understanding of how signals are transmitted through the MAP kinase pathway, we applied a multi-disciplinary approach, combining cryo-EM with molecular dynamics simulations and cellular assays, to characterize a complex between the MAP kinase p38α (MAPK14) and its activating MAP2K MKK6 (MAP2K6). Here, we present the first detailed molecular model of this highly dynamic and transient interaction between signalling components, providing insights into specificity and multi-step catalysis. Our findings open potential new routes to drug development for the important MAPK signalling pathway, and also lead to a better understanding of a crucial step in kinase signalling cascades.

Engineering an active and stable MKK6-p38α complex for structural studies

The MAP kinases are malleable proteins that have to adapt to multiple upstream and downstream effectors, as well as phosphorylating a large range of substrates. The proteins must therefore adopt multiple conformations and, crucially, interactions with effectors and substrates must be transient in order to maintain signal transmission. In order to stabilise the complex for structural studies, we created a chimera of MKK6, named MKK6^{DD}GRA, where we replaced the native KIM with that from the *Toxoplasma gondii* effector protein GRA24 (*28*) that has a 100-fold higher affinity for p38α (*29*). We also inserted phosphomimetic mutations in the MKK6 A-loop (S207D and T211D) (Fig. 1A and S1). Analysis by small angle X-ray scattering (SAXS) showed significant heterogeneity in the size of the complex formed with p38α (Fig. S2A). By screening MKK6^{DD}GRA with a combination of different nucleotide analogues and p38α A-loop mutants, we identified the mutant p38α^{T180V} (one of the residues phosphorylated in the A-loop), in combination with the transition state analogue ADP.AlF_4^-, as the complex with the smallest radius of gyration (Rg) (Table S1).

Architecture of the MKK6-p38α complex

We imaged the 80 kDa MKK6^{DD}GRA-p38α^{T180V} complex by cryogenic electron microscopy (cryo-EM) (Fig. 1). The purified complex was well dispersed and yielded 2D class averages that showed clear secondary structure features (Fig. 1B). The selected particles allowed the 3D reconstruction to a nominal resolution of 4 Å (map range 2.7-6.5 Å, Fig. 1C and S3, Movie S1). The final resolution was limited not only by the small size of the complex, but also by the highly dynamic nature of the interaction between the kinases, leading to particle heterogeneity. Therefore, very strict selection of particles was necessary to capture this conformation.

The model was initially built by docking previously determined crystal structures of both kinases within the density. We then computed the cross-correlation between experimental and predicted maps for structures obtained from molecular dynamics and modelling to select the model that best recapitulates the available data (Fig. 1D and S3C, Tables S2 and S3). The reconstruction shows the kinases adopting a 'face-to-face' conformation with most contact between the C-lobes. MKK6 is in the active kinase conformation based on its αC-helix rotated position (Fig. S4) and density can be observed for nucleotide in its active site (Fig. S5). The p38α A-loop is ordered and extends toward the MKK6 active site; however, it remains dynamic, limiting the resolution of this region (Fig. S5). The p38α active site also binds nucleotide (Fig. S5) implying it is already in an active conformation. MKK6 interacts with the p38α docking site through the GRA24 KIM at the start of its N-terminal extension that can be traced in the density (Fig. 1C and S5). Most of the linker between the KIM and the MKK6 kinase core, as well as MKK6 A-loop, remains disordered and therefore unresolved.

The main kinase core fold interaction is between the αG-helix (residues 262-273) of MKK6 and a hydrophobic pocket in p38α partly formed by the MAPK specific insert in the C-lobe (Fig. 2A, C and D, Movie S2). This insert has been described as a lipid binding site important in regulation (*30, 31*) and several studies have identified small molecules that target this pocket (*32-36*) (Fig. S6). Recently, it has also been shown to be important in substrate binding (*37, 38*), where a helix from the p38α substrate ATF2 binds in a similar manner (Fig. S6). The exposed residues of this helix, as well as residues lining the MAPK hydrophobic pocket, are highly conserved in the MAP2Ks and MAPKs respectively, suggesting a common interaction site for the pathways (Fig. 2E). Additionally, there is a potential interaction between the N-lobes via the loop between the β3-sheet and αC-helix of MKK6 (residues 87 to 89) and β-strands 1, 2 and 3 of the N-lobe of p38α (Fig. 2B). To study the importance of these interactions

on p38α activation we mutated the MKK6 αG-helix residues facing the p38α hydrophobic pocket to alanine (F264A, Q265A, L267A, K268A, E272A – referred to as MKK6^{DD} αG-helix mutant) and also the β3-αC loop of the MKK6 N-terminal interaction to alanine residues (T87A, V88A, N89A – referred to as MKK6^{DD} β3-αC loop mutant) and read out the effect on signalling *in cellulo* using a reporter luciferase assay (Fig. 2F). We transiently transfected HEK293T cells with p38α and MKK6^{DD} mutants, together with a plasmid encoding firefly luciferase under the control of the AP-1 promoter, where AP-1 activity is stimulated by p38α via several substrates (e.g. ATF2, see Materials and Methods). The MKK6^{DD} αG-helix mutant reduced the activation of p38α by 70% when compared to MKK6^{DD}, demonstrating the important role this interaction plays in the stability of the complex and activation. The MKK6^{DD} β3-αC loop mutant increased activity to ~170% over MKK6^{DD}. This loop is the site of numerous activating mutations, particularly in cancer, that stabilise the 'αC-in' conformation (*39, 40*). This could explain the observed increase in signalling, but does not rule out a role of the p38α N-lobe in the stabilisation of the active conformation of MKK6 in the face-to-face complex.

The N-terminal extension of MKK6 remains mainly disordered and its length and secondary structure elements contribute to pathway specificity

There is a wealth of data on interactions between KIMs and MAPKs, but the role of the remainder of the N-terminus is poorly understood (*41, 42*). The MAP2Ks MEK1 and MKK7 contain a regulatory helix between their KIMs and the kinase core fold (*16, 43, 44*) (Fig. 3). MKK7 also presents two short extra β-strands completing the N-lobe β-sheet of the kinase core after the regulatory helix, a feature that is also predicted for MKK6, MKK3 and MKK4 by AlphaFold2 (*45*) (Fig. 3C). This extended β-sheet fits into our reconstruction (Fig. 1C and S5). We do not observe density beyond this element, presumably because most of the N-terminus

remains disordered. In our cryo-EM map, the engineered KIM is clearly visible (Fig. 1C and S5), but it does not appear to interact further with p38α. To investigate whether the N-terminal extension has a role beyond simply associating the kinase to the KIM, we again used the luciferase reporter assay to test the role of the MKK6 N-terminus in activating p38α. We produced constructs that scan the region between the KIM and the first consensus β-sheet of the kinase core with alanine blocks in order to determine if there is sequence specificity or direct interaction with p38α (Fig. 3D). Our results show that the sequence of the middle region ($MKK6^{DD}$ Ala scan 28-39) of the N-terminal linker has no effect on p38α signalling *in cellulo*. However, the sequence of the linker close to the KIM ($MKK6^{DD}$ Ala scan 18-29) and the region close to the kinase core, which comprises the predicted β-strands ($MKK6^{DD}$ Ala scan 38-49) seem to have some importance as their mutation to alanines reduced p38α signalling by 27% and 58% respectively.

While KIM sequences are important, they do not sufficiently explain specificity. Comparing the N-terminal linkers of the MAP2Ks, they differ significantly in their length and secondary structure elements (Fig. 3B and C), could this contribute to specificity between the pathways? When we substituted the MKK6 linker with those from the MAP2Ks of the other pathways, activity is significantly reduced (Fig. 3D). This is most drastically observed with the linkers from MEK1 and 2. Even the linkers from MAP2Ks that activate p38α see reduced activity and are not sufficient to rescue the activation, even though the KIM, MAP2K and MAPK are in the correct combination. Moreover, our reconstruction implies that the length of the linker is just sufficient to allow the observed interactions between the kinases, in particular the MAP2K αG-helix position relative to the MAPK hydrophobic pocket formed by the MAP kinase insert. By removing or adding 10 residues to the linker region, activity is reduced by ~50%. This implies that the length of the linker, controlled by either the number of amino acids

and/or secondary structure elements, is important in the positioning of the MAP2K for engagement with the MAPK, and is finely tuned for MAP kinase pairs. The specificity of a MAP2K is therefore defined by cooperation between the KIM, the linker and the kinase core itself.

Molecular dynamics show the complex is metastable but that a catalytically competent state can be formed

Given the highly dynamic nature of the kinase interaction, resulting in heterogeneity and moderate resolution of the cryo-EM data, we carried out a series of molecular dynamics (MD) simulations to better understand the details of the transphosphorylation of p38α on T180 and Y182 by MKK6 in the face-to-face complex (Table S6). We ran a set of simulations, either with or without restraints between the kinases, starting from models derived from the cryo-EM structure: MKK6GRA-p38α with the WT A-loop, and MKK6-p38α, where we reverted the sequence of the A-loop and the GRA24 KIM back to the WT.

In most of the simulations, the contact between the KIM and p38α was retained. In some cases, a partial detachment of p38α from MKK6 was observed. We also observed a number of "rotated" complexes (discussed below). Finally, in some simulations, conformations not compatible with catalysis were observed. This variety is not unexpected given the heterogeneity observed when preparing the complex for structural studies, which is indicative of the transient nature of the interaction of the two kinases. Thus, we also ran simulations with mild restraints at the interface to increase the sampling of the A-loop and other flexible regions in the face-to-face catalytically competent dimer orientations (see supplementary text). In accordance with the 70% decrease in activity seen in the $MKK6^{DD}$ αG-helix mutant (Fig. 2F), the MD simulations indicate a significant role of a hydrophobic patch and a network of hydrogen bonds located at the interface of the C-lobes of the two kinases in keeping them together. In all simulations in which

the two kinases break apart, this tight hydrogen-bonding network is the last point of contact to be lost. In particular, the αG-helix of MKK6 (residues F264-E272) is involved in interacting with p38α and stabilising the complex. The interaction between MKK6 K268 and E272 and p38α S261 seems to be one of the main interactions keeping the two kinases in close proximity (Fig. 2G).

With respect to the phosphorylation mechanism, in a number of instances, either p38α T180 or Y182 approached the MKK6 ATP at a catalytically competent distance (the distance of the OH group of p38α T180 or Y182 and the γ-phosphate group of MKK6 bound ATP was comparable to that observed in the phosphorylation of the SP20 substrate by PKA (*46*)) (Fig. 4 and Table S7). In particular, in the simulations of MKK6-p38α (WT KIM) both T180 and Y182 come close to the catalytic site. While in the simulations of MKK6GRA-p38α, we observe a number of "rotated" complexes where T180 is preferentially close to the catalytic site (see below). In the catalytically competent conformations, we observed that in most cases p38α Y182 reached the MKK6 ATP before T180.

The tendency of monomeric, unphosphorylated p38α to adopt inactive, sequestered, A-loop conformations has been extensively shown in previous studies (*47*). Thus, the observation that in the simulated complex the unphosphorylated A-loop of p38α adopts an exposed conformation in multiple instances in proximity to the catalytic site of MKK6, is indicative of an active role of MKK6 in stabilizing such conformations. The active role of MKK6 is further confirmed by the fact that in one of the "released" simulations, initiated from a frame showing the p38α Y182 close to MKK6 ATP, we observe a series of events starting with the MKK6 KIM detaching, which in turn destabilises the complex and leads to the separation of the two kinases. After the separation, the p38α A-loop transitions from an exposed to sequestered

conformation (Fig. 5). This is consistent with the importance of the KIM in stabilising the dimer and the importance of the complex in stabilising extended conformations of the A-loop.

A rotated complex might facilitate the phosphorylation of p38α T180

In one of the MD unrestrained simulations of MKK6GRA-p38α, we observe T180 approaching the γ-phosphate of ATP in the catalytic site of MKK6 from an unexpected angle, where the p38α N-lobe underwent a large conformational change that resulted in a 77° rotation around its axis (Fig. 6A, Movie S3). In this conformation, p38α was kept close to MKK6 through the KIM, despite the rotation. Interestingly, the KIM of MKK6 seems to play a key role, not only in maintaining the two kinases close together, but also in facilitating the rotation of p38α. Particularly, before T180 gets close to the ATP, a key lysine located just after the KIM, K17, forms a salt-bridge with p38α E160 which seems to initiate the rotation of p38α (Fig. 6B). In two of the "released" simulations, we also observe the p38α N-lobe rotation (by 51° and 66°, respectively) and concurrent proximity of T180 with MKK6 bound ATP (Movie S3).

The rotated complex was validated by comparing one of the rotated conformations extracted from clustering the relevant trajectory against SAXS data. The SAXS data clearly indicate that in the presence of AMP-PCP, the complex is highly flexible and dynamic with Rg in the 39 to 40 Å range compared to the more compact values obtained with the transition state analogue ADP.AlF_4^-, where the face-to-face conformation is stabilised. The most compact state is the p38α^{T180V} complex (29.6 Å) followed by p38α^{WT} (32.2 Å) and p38α^{Y182F} (35.3 Å) (Table S1 and Figure S2). The theoretical Rg for the rotated conformation is larger than the p38α^{T180V} complex corresponding to the face-to-face dimer.

To validate the functional relevance of this rotated intermediate observed in the simulations, we carried out site-directed mutagenesis where we mutated the key lysine K17 to alanine. Interestingly, the MKK6$^{DD\text{-}K17A}$ leads to 26% increase in activity as measured by downstream signalling (Fig. 6C). The mutation is expected to abolish the K17-E160 salt bridge that primes the complex towards the rotated orientation (and T180 phosphorylation). As discussed below, we expect that by suppressing the rotated complex, the mutant could favour the formation of face-to-face dimers and enhance the more efficient phosphorylation pathway of Y182.

Discussion

Initial docking

The N-termini of the MAP2Ks contain a conserved KIM motif that is required for binding to MAPK substrates. The first step in activation is KIM binding, and in our structure, the KIM of MKK6 is in contact with the known docking site of p38α. During the MD simulations, KIM binding was seen to induce allosteric changes in p38α that adopts a prone-to-be-phosphorylated conformation with its A-loop extended, exposing the tyrosine and threonine residues, in agreement with crystal structures. However, the KIM only partially explains the strength and specificity of the interaction between a MAP2K and its substrate MAPK (*48*). Our data indicate that the interaction between MKK6 N-terminus and p38α extends beyond the hydrophobic residues of the KIM and is important in the activation process. Although most of the MKK6 N-terminal linker remains disordered, its length seems to be tightly linked to the substrate MAPK and the presence of some secondary structural elements differs between MAP2Ks contributing to specificity (Fig. 3C). Comparison with other MAP2K-MAPK dimers could reveal the implications of this region in the specificity of the pathways. In the structure

presented here, MKK6 is in the active conformation, whilst all crystal structures of MKK6 solved so far are in the inactive conformation, even in the presence of activating mutations of the A-loop and nucleotide binding (Fig. S4). Once p38α is recruited, some parts of the MKK6 N-terminal linker could participate in the conformational shift towards the MKK6 active conformation, but its main function appears to be to prepare the MAPK A-loop and guide the engagement with the αG-helix.

Engagement with substrate

We show that the predominant interaction for activation is mediated by the αG-helix of the MAP2K MKK6 and the p38α hydrophobic pocket formed by the αG-helix of p38α and the specific MAPK insert. This region is also important in MAPKs for substrate recognition (*37*) and interaction with scaffold proteins and downstream regulators such as phosphatases (*27*, *38*, *49*). The engagement of αG-helices seems to be an emerging theme in kinase heterodimers: only a few structures have been determined, such as the KSR2-MEK1 heterodimer (*27*) and more recently, the BRAF-MEK1 complex (*25*), both upstream components of the related ERK MAPK pathway. In both these structures the αG-helices interaction is very similar, as well as the relative orientation of the kinases. Several studies have shown that small molecules can target this region (*32*-*36*) and modulate the position of the MAPK insert helices (Fig. S6). However, as the pocket is very deep, the molecules may not extend far enough to disrupt the interactions identified here. There has been intense interest, and some success (*50*), in developing drugs that target p38α, mostly binding to the nucleotide pocket, but they have been mired by off target and toxicity effects (*9*). The molecules that have been identified as binding to the MAPK insert pocket could be further developed to better disrupt both the MAP2K interaction, and that of substrates, that could lead to highly specific p38 inhibitors.

The MKK6 KIM–p38α docking site, the MKK6 N-terminal linker, and the MKK6 αG-helix–p38α hydrophobic pocket interactions, are clearly essential for defining the specificity of the kinase-substrate interaction, for positioning the two kinases, and for triggering the necessary changes towards the MKK6 active kinase conformation and positioning the A-loop of p38α to be accessible for phosphorylation. Our data demonstrate that altering any of these three components perturbs activation of downstream signalling.

Freedom of interaction at the catalytic centre

All contacts observed between the kinases are distal to the active site, explaining the lack of sequence specificity or conservation in MAPK A-loops in the region preceding the TxY motif (*44*). Rather than the active site of a classical enzyme, where substrates are perfectly positioned for catalysis, the MAP2K/MAPK complex appears to provide a zone of proximity, allowing the flexible activation loop to move, but increasing the probability, or local concentration, of the p38α T180 and Y182 residues to be positioned next to the γ-phosphate of ATP. Dual specificity MAP2Ks are unusual as the two amino acids targeted are significantly different to each other, when compared to serine/threonine kinases. In addition, the two substrate phosphorylation sites are only one residue apart and the MAP2Ks need to have an active site that can accommodate, effectively, 4 substrates (A-loop **T**-x-Y; T-x-**Y**; **T**-x-Y^P; T^P-x-**Y** (targeted residue in **bold**)), all with significantly different sizes and charges. This implies that flexibility in the active site is essential in order to accommodate such a wide variety of substrates. By not binding any residues of the activation loop specifically, the various different residues and phosphorylation states could be accommodated by sacrificing catalytic efficiency for flexibility.

The MD simulations revealed that the face-to-face architecture of the hetero-kinase dimer of our model is compatible with the phosphorylation of either T180 or Y182 of the p38α A-loop

(Fig. S7). Another conformation, where p38α rotated, emerged, and seems to favour the phosphorylation of T180. Kinetic data have shown that the dual-phosphorylation of p38α by MKK6 involves a partially processive mechanism *in vitro*, in which the monophosphorylated intermediates can either dissociate from the enzyme or proceed to the next catalytic step. Wang *et al. (51)* and others (*52*) proposed that both p38α monophosphorylated forms can be produced by MKK6 catalysis with a preference for Y182, whose phosphorylation is four-fold faster than that of T180. With respect to the second catalytic step, the experimentally measured kinetic rates indicate that phosphorylation at Y182 in the first step enhances the catalytic efficiency of MKK6 phosphorylation at T180 in the second step. According to our simulations (Fig. 6 and S7), when the N-lobe of p38α undergoes a large conformational change towards the rotated dimer, T180 is in the right position to be phosphorylated, while Y182 is more distant from the catalytic site, which might explain the observed lower catalytic efficiency of MKK6 when the second phosphorylation is on Y182 by kinetic measurements. Conversely, Y182 seems to be able to easily approach MKK6 ATP in the face-to-face catalytically-competent conformations and then be phosphorylated. Thus, the difference in the experimental kinetic rates measured for the first phosphorylation step may reflect the rotation of p38α N-lobe around its axis that seems to be involved in the T180 phosphorylation only. The partial processivity of the dual-phosphorylation in a cellular context remains an open question (*53, 54*), but the architecture of the interaction between MKK6 and p38α seems to be compatible with either a distributive, partially processive or fully processive mechanism.

By combining cryo-EM and MD simulations, together with structure-driven mutagenesis *in cellulo*, we describe the range of attributes that lead to MKK6 selectivity and p38α activation as well as identify potential new druggable sites for this medically important complex.

Furthermore, our data describe the first molecular details of the activation of one protein kinase by another – one of the most fundamental mechanisms in cell signalling.

Materials and Methods

Plasmids

Plasmids were ordered from GenScript (gene synthesis, cloning and mutagenesis). For recombinant protein expression, human p38α sequences (WT, T180V and Y182F mutants) were fused to a His6 tag with a 3C protease cleavage site and cloned into a pET-28b vector; $MKK6^{DD}$GRA sequence (constitutively active S207D T211D mutant of human MKK6 with GRA24 KIM) was fused to a twin StrepII tag with a 3C cleavage site and cloned into a pFastBac1 vector. For cellular reporter assays, p38α and $MKK6^{DD}$ mutants sequences were cloned into pcDNA3.1 plasmids. The lambda Phosphatase plasmid was obtained from Addgene (a gift from John Chodera & Nicholas Levinson & Markus Seeliger; Addgene plasmid # 79748 ; http://n2t.net/addgene:79748 ; RRID:Addgene_79748) (*55*).

Protein expression and purification

Constructs of p38α were co-transformed with the lambda phosphatase plasmid into Rosetta™(DE3)pLysS *E. coli* competent cells (Novagen) with appropriate antibiotics. Cells were grown in LB at 37°C until the OD600 = 0.6-0.8, induced with 0.5 mM IPTG, incubated at 16°C overnight, and harvested by centrifugation.

The $MKK6^{DD}$GRA construct was transformed into DH10 *E. coli* cells to produce recombinant baculoviruses subsequently used for protein expression in *Sf21* insect cells (*56*). Cells were harvested 48h after proliferation arrest by centrifugation.

Cell pellets were resuspended in lysis buffer (50 mM HEPES pH 7.5, 200 mM NaCl, 10 mM $MgCl_2$, 5% glycerol, 0.5 mM TCEP, with a Pierce protease inhibitor EDTA-free tablet (Thermo Scientific) and a trace of DNaseI (Sigma)). Cells were lysed by sonication on ice and the lysate centrifuged.

For p38α, supernatant was loaded onto a pre-packed 5 ml HisTrap column (GE Healthcare), equilibrated according to the supplier's protocols with wash buffer (50 mM HEPES pH 7.5, 200 mM NaCl, 10 mM $MgCl_2$, 5 % glycerol, 0.5 mM TCEP) with 1% elution buffer (wash buffer with 500 mM Imidazole). Tagged-protein was eluted with elution buffer and p38α-containing fractions were pooled, incubated with 3C-protease and dialysed against wash buffer at 4°C overnight. The sample was run through the HisTrap column again to remove uncleaved protein and flow-through fractions were collected.

For $MKK6^{DD}GRA$, supernatant was loaded onto a pre-packed 5 ml StrepTactin XT column (IBA), equilibrated according to the supplier's protocols with wash buffer. Tagged-protein was eluted with elution buffer (wash buffer with 50 mM Biotin), and MKK6-containing fractions were pooled, incubated with 3C-protease and dialysed against wash buffer at 4 °C overnight. The sample was run through the StrepTactin XT column again to remove uncleaved protein and flow-through fractions were collected.

Pure proteins were concentrated using 10 kDa Amicon Ultra membrane concentrators (Millipore), flash-frozen in liquid nitrogen and stored at -80℃.

In order to prepare the hetero-kinase complex, $MKK6^{DD}GRA$ and p38α aliquots were thawed, mixed in 1:1 mass ratio and incubated on ice for 1h. The sample was then concentrated to 10 mg/ml with a 10 kDa Amicon Ultra membrane concentrators (Millipore) and loaded onto a Superdex S200 increase 10/300 GL size-exclusion column (GE Healthcare) equilibrated in wash buffer (with a reduced glycerol concentration of 2% when for cryo-EM studies). Purest peak fractions were pooled, flash-frozen in liquid nitrogen and stored at -80℃ before being used for structural studies or biochemical assays.

SAXS

Purified MKK6^{DD}GRA-p38α complexes were complemented with either 10 mM ADP, 10 mM NH_4F and 1 mM $AlCl_3$ or 10 mM AMP-PCP, and incubated on ice for 30 minutes before proceeding.

Small Angle X-ray Scattering data were collected at the bioSAXS beamline B21 at the Diamond Light Source (DLS), UK (proposal SM23091-1). Scattering curves were measured from solutions of the different MKK6DDGRA/p38α samples in SAXS buffer (50 mM HEPES pH 7.5, 200 mM NaCl, 10 mM MgCl2, 5 % glycerol, 0.5 mM TCEP). Buffer subtractions and all other subsequent analysis were performed with the program Scatter IV (*57*) and SAXS profile computation used FoXS (*58*) (Table S9).

Cryo-EM specimen preparation and data collection

Purified MKK6^{DD}GRA-p38α^{T180V} was complemented with 250 µM AMP-CP, 250 µM NH_4F and 25 µM $AlCl_3$, and incubated on ice for 30 minutes before proceeding. UltraAufoil 1.2/1.3 grids were glow-discharged for 30 seconds at 25 mA (PELCO easy glow). During the vitrification procedure on a Vitrobot Mark IV (FEI), 4 µl of sample at 6 µM concentration was applied to the grid. The blotting force was set to 0 for a total time of 3.5 seconds. Grids were then clipped and screened on a FEI Talos Glacios electron microscope (EMBL Grenoble) operating at 200 kV. Selected grids were then sent for data collection on a FEI Titan Krios (EMBL Heidelberg) operating at 300 kV. Micrographs were automatically collected using SerialEM (*59*) from a K2 Quantum detector (Gatan) and a GIF Quantum energy filter (Gatan), at a nominal magnification of 215 kx (corresponding to 0.638 Å/pixel at the specimen level). Three different data collections with a total of 28,633 movies of 40 frames were collected in electron

counting mode with a defocus range of -1.5 to -3 µm, 0.1 µm step, with a total exposure of 62.77 $e^-/Å^2$.

Cryo-EM processing

Each dataset was treated independently following a similar workflow and the best particles corresponding to the hetero-kinase sample were finally combined and further processed.

Movies were imported in cryoSPARC (*60*). All movie frames were aligned and motion-corrected with Patch Motion correction and CTF estimated with Patch CTF. Data were manually curated to eliminate micrographs with large motions, poor resolution, and high ice thickness. The resulting micrographs showed a low signal/noise ratio but classical picking with blob picker failed to identify particles. We successfully picked a large number of particles by using a combination of Topaz particle picker (*61*) and template picker. Particles were extracted with a box size of 300 x 300 pixels and 2D classification was used to eliminate junk and the most noisy particles. We then applied *ab-initio* and heterogeneous refinement, requesting 3-6 models, and particles corresponding to the hetero kinase model were selected for further 2D classification. Between 2-3 rounds of 2D classification were necessary to select good particles, showing secondary structural features and low background noise. Non-uniform refinement was then use to obtain a 5 Å resolution map. An exemplary workflow is shown in Figure S3A for dataset 2.

To improve resolution, we then combined selected particles form each dataset (86,510 particles in total) and we applied 2D classification, *ab-initio*, heterogeneous and non-uniform refinement to obtain a final map at 4.00 Å resolution, corresponding to 35,123 particles (Fig. S3B). Maps were sharpened in cryoSPARC and using locscale (*62*).

The initial model was built from the combination of different structures: the crystal structure of p38α WT presenting an ordered activation loop (PDB 5etc), the crystal structure of

p38α bound to GRA24 KIM peptide (PDB 5eta) (*29*), and the homology model of MKK6^{DD} based on the crystal structure of the active MKK7^{DD} structure (PDB 6yg1) (*16*) obtained with SWISS-MODEL (*63*). The model of each kinase was individually docked into the map as a rigid body using phenix.place.model and then refined with one round of morphing and real space refinement using Phenix (*64*) and corrected in COOT (*65*). To validate the rebuilt model, we relied on cross-correlation calculations between the experimental maps and those predicted from the MD simulations to select the model that best recapitulates the available data. We considered a set of 87 structures including the rebuilt model, AF2 predictions, complex structures including the linker and p38α activation loop modelled using the *automodel* functionality of MODELLER, and 79 clusters extracted from one relevant MD simulation showing p38α Y182 close to MKK6 ATP (rep4 with restraints). Given the sensitivity of cross-correlation calculations to atomic B-factors, we re-assigned temperature factors for each structure using Phenix by running one round of refinement with default parameters. This step allowed us to compare the cross-correlation scores assigned to all the models in the dataset. Cross-correlation scores were then computed considering the entire complex and a selection of key structural features, i.e., hydrophobic patch, KIM, p38α activation loop, and the MKK6 region close to the resolved linker. By selecting a specific region of the structure, cross-correlation was computed in the area surrounding the selection only. Considering the entire complex, the rebuilt model was assigned to the highest cross-correlation score. However, one of the predicted models was assigned to a higher score than the rebuilt model for the area around the hydrophobic patch, the p38α activation loop, and the MKK6 region close the linker. We therefore incorporated the structural information for these features into the final model as they are in better agreement with the experimental data. Table S2 summarizes the cross-correlation scores for all structures. See Table S3 for data processing and

refinement statistics. Figures were prepared in ChimeraX (*66*) and validation performed with Phenix Comprehensive Validation.

AP-1 reporter assay

HEK293T cells were maintained in DMEM medium (DMEM) supplemented with 10% (v/v) FBS (Thermo Fisher), at 37 °C and 5% CO_2. According to the manufacturer's protocol, the AP-1 firefly luciferase reporter vector and the constitutively expressing *Renilla* luciferase vector (BPS Bioscience #60612) were transiently co-transfected together with $MKK6^{DD}$ mutants and p38α pcDNA3.1 plasmids (or empty vector for controls) with Lipofectamin2000 (Thermo Scientific) (Fig. S8). Firefly and *Renilla* luciferase activities were measured 24h post-transfection using the Dual Luciferase assay system (BPS Bioscience #60683) with a Clariostar microplate reader (BMG Germany). Each experiment was repeated three times (biological replicate) and each time, three transfections per condition were performed (technical replicate), for a total of nine experiments per construct. Each firefly luciferase value was normalised by its corresponding *Renilla* luciferase measure to correct for cell quantity and transfection efficiency. The luciferase activity was expressed relative to the replicate positive control ($MKK6^{DD}$ + p38α) intensity. Statistical analysis on the AP-1 reporter assay was performed using Rstudio. Briefly, normal distribution was tested with a Shapiro Wilck test and variance homogeneity with a Levene's test. To compare the mutants to the control ($MKK6^{DD}$ + p38α), either a Welch t-test or a Wilcoxon rank sum exact test was performed.

Mass spectrometry

Purified MKK6^{DD}GRA-p38α complexes were complemented with 10 mM ATP. Intact mass was measured on a quadrupole time of flight (Q-TOF) Premier mass spectrometer (Waters/Micromass) coupled to an Acquity UPLC System (Waters Corporation). Solvent A was water, 0.1% formic acid, and solvent B was acetonitrile, 0.1% formic acid. Samples were acidified using 1% TFA prior to injection onto an Acquity UPLC Protein BEH C4 column (Waters Corporation). Acquisition was carried out using the standard ESI source in positive ion mode over the mass range 500–3500 m/z. Data were externally calibrated against a reference standard of intact myoglobin, acquired immediately prior to sample data acquisition. Spectra from the chromatogram protein peak were then summed and intact mass was calculated using the MaxEnt1 maximum entropy algorithm (Waters/Micromass).

PTMs were measured by LC-MS/MS. SP3 protocol (*67*) was used for sample preparation. Analysis was performed on an UltiMate 3000 RSLC nano LC system (Dionex) fitted with a trapping cartridge (µ-Precolumn C18 PepMap 100) and an analytical column (nanoEase™ M/Z HSS T3 column 75 µm x 250 mm C18, 1.8 µm, 100 Å, Waters) coupled to a Fusion Lumos (Thermo) mass spectrometer using the proxeon nanoflow source in positive ion mode. Acquired data were processed by IsobarQuant (*68*), as search engine Mascot (v2.2.07) was used.

Protein structure preparation for MD simulations

The model derived from cryo-EM of p38α in complex with the MKK6^{DD}GRA was used as a starting conformation for the unbiased MD simulations. The bound ADP that was resolved in the cryo-EM structure was replaced by ATP, which was docked to the binding sites of p38α and MKK6 using the Glide software (*69*) (Schrödinger Release 2021-4). In particular, the docked ATP maintained the ADP pose seen in the cryo-EM structure, while the position of AlF_4^- in the binding site of p38α was used to guide the position of the γ-phosphate group of the docked ATP.

The same γ-phosphate position was used for the ATP in the binding site of MKK6, even though AlF_4^- was not present in this binding site. The mutated residues S207D and T211D on the resolved $MKK6^{DD}$ were reverted back to the WT ones. The K53R mutation was introduced unintentionally when building the model of p38α with the WT KIM, as this was the mutant used in the crystal structure. It is a kinase dead mutation that stabilizes the protein for structural studies, but has no influence on the studies presented here. The structure of the p38α-MKK6GRA produced by the aforementioned procedure was then used to model the N-terminal tail of the WT MKK6 (residues M1-K14 of the MKK6 WT sequence) using the crystal structure of p38α bound to the WT MKK6 KIM (*29*) and with the *automodel* functionality of MODELLER (*70*).

MD simulations setup

Prior to any simulation, the protonation state of each residue at pH 7.4 was calculated using the PROPKA 3.1 algorithm as implemented in the PlayMolecule web application (*71*), which left all residues in their usual charge states, except for p38α H228, which was double protonated. For all simulated systems, DES-Amber force field was used for the protein as it has been shown to be able to capture the dynamics of protein-protein complexes more accurately than other force fields to this date (*71*). For the ATP coordinated Mg^{2+} ions, optimized Mg force field parameters that yield water exchange on timescales that agree with experiments (*71*) were combined with the protein force field. The Meagher et al. parameterization for ATP (*72*) was used, as these parameters have been benchmarked recently and shown to be able to reproduce the experimentally observed coordination modes of ATP (*73*). Each system was enclosed in an octahedral box with periodic boundary conditions and solvated with TIP4PD water molecules as

described in the DES-Amber force field, while Na^+ and Cl^- ions were added to reach neutrality at the final NaCl concentration of 150 mM.

The MD simulations were performed using the GROMACS 2021.3 simulation package (*74*) patched with the PLUMED 2.4.1 plug-in (*75*). The energy of the MKK6GRA-p38α and MKK6-p38α systems was minimized using the steepest descent integrator and the solvated systems were equilibrated afterwards in the canonical (NVT) ensemble for 10 ns, with initial velocities sampled from the Boltzmann distribution at 310 K and a 2 fs timestep. The temperature was kept constant at 310 K by a velocity-rescale thermostat (*76*). The long-range electrostatics were calculated by the particle mesh Ewald algorithm, with Fourier spacing of 0.16 nm, combined with a switching function at 1.0 nm for the electrostatic and VdW interactions. The systems were then equilibrated for additional 10 ns in the isothermal-isobaric (NPT) ensemble prior to the production runs applying position constraints only to the protein (with a restraint spring constant of 1000 kJ mol^{-1} nm^{-2}), where the pressure was maintained at 1 bar through a cell-rescale barostat (*77*).

Post equilibration, we ran a series of independent production runs in the NPT ensemble, coupled with a velocity-rescale thermostat (*70*) at 310 K and a cell-rescale barostat (*77*) at 1 bar for each of the systems as detailed in Table S6. Both unrestrained and restrained sets of replicas for MKK6GRA-p38α are randomly initialized from the same initial conformation and differ by the application of a harmonic restraint on the distance to the native inter-kinase contact found at the interface of the two monomers to maintain the initial relative position of p38α and MKK6GRA. The distance to the native contact map as implemented in the PLUMED plug-in was restrained using a force constant of 1500 kJ mol^{-1} nm^{-2}. Since the movement of the A-loop of p38α was important, contacts that involved residues of the A-loop were removed from the final contact map. The definition of the atoms involved in each contact, as well as the parameters for

the contact map can be found in the input files deposited to the public repository of the PLUMED consortium, PLUMED-NEST (*78*).

We expanded the dataset of unrestrained simulations for MKK6GRA-p38α adding a set of three replicas starting from a conformation that originates from a snapshot of one of the restrained simulations in which the A-loop of p38α extended towards MKK6 ATP binding site and p38α Y182 was close to MKK6 ATP.

MD simulations derived structures and analysis

In order to quantify the rotation of p38α with respect to MKK6 over the course of the simulations, we started by clustering the conformations derived from each MD simulation run. All the conformations visited during each simulation were clustered using the *gromos* algorithm (*79*) and the *g_cluster* routine (GROMACS) by using the RMSD of the backbone atoms of MKK6 as the distance between the structures and the cut-off value from 2 to 4.5 Å to ensure a representative number of frames in each cluster. The central structures of the most populated clusters of each basin (i.e. the structure with the smallest RMSD distance to all the other members of the cluster) were chosen as the representative ones of each simulation. The central structures of each simulation were then superimposed to the cryo-EM structure using the MKK6 as reference and the rotation matrix of p38α was calculated through the ChimeraX functionalities.

Supplementary Text

Unrestrained simulation of MKK6-p38α indicate that Y182 can reach MKK6 ATP

Since the resolved cryo-EM structure has a chimeric MKK6 with a modified KIM on its N-terminal tail adopted from GRA24, we reasoned that the simulations of the MKK6/p38α with the WT KIM of MKK6 could give us more information on the role of this motif that the cryo-EM structure alone could not provide. In the WT, the "electrostatic hook" of KIM is recognised by p38α and forms ion pairs with residues of the β7/β8 turn of p38α. Indeed, during the simulations, K8 and R9 of the WT sequence anchor the KIM to p38α by forming backbone and side-chain hydrogen bonds and salt-bridges with E161, while the salt-bridge between the side chains of K14 and E160 further solidifies the KIM around p38α (Fig. S9). Unlike the set of simulations with the chimeric MKK6, in two out of the five simulations of this setup, we see both T180 and Y182 coming relatively close to MKK6 ATP (Table S7) without p38α having to rotate. Both during the approaching of the A-loop of p38α to the MKK6 ATP and after, the two kinases maintain their initial relative orientation throughout the simulations.

During the simulations of p38α with MKK6 comprising of the WT sequence we were not able to see the rotation of p38α even though T180 got relatively close to ATP in one of the replicas. We think that the simulation time may not be sufficient for the N-lobe of p38α to rotate.

Restraining the MKK6GRA-p38α relative position enhances the phosphorylation at Y182

We ran a set of five simulations for the MKK6GRA-p38α dimer starting from the cryo-EM structure and applying mild harmonic restraints on the interface interactions to stabilise the relative orientation of the monomers in the complex (see Methods). Due to the presence of the restraints, we did not observe any large conformational change akin to the one seen in the

unrestrained simulation described in the Main Text showing T180 clearly interacting with MKK6 ATP.

In this set of restrained simulations, two out of the five replicas show p38α A-loop adopting an extended conformation with Y182 approaching P_γ of MKK6 ATP up to a final distance of 4.4 Å and 3.5 Å, respectively. In both cases, p38α ATP binding site slightly opens allowing the adenine group of p38α ATP to move out of the binding site. Interestingly, in one of the two simulations, we also see that the extended A-loop forms a one-turn helix (residues E178-Y182), which involves both phosphorylation sites. A similar transient helix on the middle section of the A-loop, which exposes the phosphorylation sites, has been reported in MD simulations of the unphosphorylated kinase domain of EGFR (*80, 81*), and is also reminiscent of a helix in the A-loop of MPSK1 kinase (*82*) (PDB 2buj). In the rest of the replicas of this set of simulations, the conformation adopted by the A-loop is not compatible with phosphorylation on either T180 or Y182 since the A-loop extends towards the p38α C-lobe or the MKK6 αC-helix.

It is worth mentioning that in all restrained simulations the KIM never detaches from p38α regardless of the relative conformation – catalytically-compatible or not - adopted by the two kinases.

<u>Released simulations of MKK6GRA- p38α confirm the role of MKK6 KIM in stabilising the active complex</u>

The results obtained from the set of restrained simulations suggest a role of MKK6 KIM in stabilizing the MKK6-p38α complex. However, due to the presence of the harmonic restraints on the interface contacts we were not able to evaluate to what extent MKK6 KIM contributes to the rotation of p38α N-lobe.

We thus ran an additional set of three simulations releasing the restraints on the interface. We started the simulations from a representative conformation of the complex extracted from one of the restrained simulations showing Y182 pointing towards the MKK6 ATP (Y182-P_γ=5.1 Å) and residues E178-Y182 of the A-loop folded into a one-turn helix.

In two out of three replicas the KIM remains stably in contact with p38α throughout the simulation.

Concurrently, we observe that in one simulation, p38α A-loop extends above the MKK6 αC-helix in a way that allows Y182 to interact with Q93, forming, thus, a catalytically incompatible complex. In the simulation we extended up to 2 μs, we observed the unfolding of the one-turn helix of the A-loop and T180 approaching MKK6 ATP. After clustering of this trajectory (RMSD cut-off distance equal to 2.75 Å), in the most populated cluster (cluster 1), Y182 and T180 fluctuate at 1-2 nm away from MKK6 ATP while in the second most populated cluster (cluster 2) they reach at a distance <1 nm. Interestingly, in cluster 1, the p38α N-lobe is turned by approximately 51° with respect to the initial conformation, while in cluster 2, in which both Y182 and T180 are closer to MKK6 ATP, the rotation is more significant, i.e., approximately 66°. This observation is consistent with what we observed with the unrestrained simulation showing the N-lobe having to rotate in order for T180 to interact with MKK6 ATP. Although interesting, from this simulation we were not able to confirm the role of the salt bridge between MKK6 K17 and p38α E160 in priming the rotation of p38α.

Lastly, in the third simulation of this set we observed p38α A-loop moving from an extended to sequestered conformation concurrently with the dissociation of MKK6 KIM, thus confirming the role of MKK6 KIM in stabilizing the active complex. The conformational change of the A-loop required approximately 200 ns after the detachment of the KIM. Finally, even when most interface contacts are lost, the contacts around the hydrophobic patch between the C-lobes of

p38α and MKK6 are maintained. Comparing the complex conformation with a reference structure for inactive p38α (PDB 3s3i) we were able to assess the inactive-like conformation of the A-loop adopted at the end of the simulation ($RMSD_{backbone}^{p38\alpha}$= 3.5 Å with respect to the crystal structure, Fig. 5B). The KIM is also in contact with the hinge region of p38α. It is worth mentioning that during the simulations that we ran, we see that fluctuations of MKK6 are propagated through its N-terminal loop and KIM to the hinge region of p38α, affecting the stability of p38α ATP inside its pocket.

Acknowledgments:

PJ was supported by a EMBL predoctoral fellowship. We thank Stephen Cusack and Andrew McCarthy (EMBL Grenoble) for providing encouragement during this project, Wojtek Galej (EMBL Grenoble) for critical reading of the manuscript and Mohamed-Ali Hakimi (IAB, Grenoble) for introducing us to the *T.gondii* protein GRA24. We acknowledge Sarah Schneider for support in using the EM Facility at EMBL Grenoble and thank Felix Weiss, Wim Hagen and Simon Fromm for excellent data collection at the EMBL Heidelberg Imaging Centre. We thank Alice Aubert and Martin Pelosse (EMBL, Grenoble) for support in eukaryotic protein expression and the proteomic core facility at EMBL Heidelberg for mass spectrometry. SAXS data were collected at beamline B21 at Diamond Light Source, UK. We acknowledge Massimiliano Bonomi (Institut Pasteur - CNRS, France) for discussions and technical support in cross-correlation analysis. Molecular graphics and analyses were performed with UCSF ChimeraX, developed by the Resource for Biocomputing, Visualization, and Informatics at the University of California, San Francisco, with support from National Institutes of Health R01-GM129325 and the Office of Cyber Infrastructure and Computational Biology, National Institute of Allergy and Infectious Diseases. We acknowledge PRACE and the Swiss National Supercomputing Centre (CSCS) for large supercomputer time allocations on Piz Daint, project IDs: pr126, s1107.

Funding:

Swiss National Science Foundation [projects number: 200021_204795] (FLG).

Bridge [40B2-0_203628] (FLG).

Author contributions:

Conceptualization: PJ, EP, MWB

Methodology: PJ, IG and DG

Investigation: PJ, IG, DG, MT, FLG, EP, MWB

Visualization: PJ, IG and DG

Funding acquisition: FLG and MWB

Supervision: FLG, EP and MWB

Writing - original draft– PJ and MWB

Writing – review & editing: PJ, IG, DG, MT, FLG, EP, MWB

Competing interests: Authors declare that they have no competing interests.

Data and materials availability:

Accession codes: Structure of the MKK6^{DD}GRA-p38α^{T180V} complex: EMD-15233 (map; Electron Microscopy Data Bank) and PDB-8A8M (coordinates; Protein Data Bank)

Figure Legends

Fig. 1. Structure of the MKK6^{DD}GRA-p38α^{T180V} complex. (**A**) Schematic of the two protein constructs. Key regions and mutations are indicated. (**B**) Representative 2D class averages from single particle cryo-EM analysis of the MKK6^{DD}GRA-p38α^{T180V} complex. (**C**) Segmented single-particle reconstruction cryo-EM map of the MKK6^{DD}GRA-p38α^{T180V} complex, resolved to 4 Å resolution and coloured according to (A). (**D**) Model of the MKK6^{DD}GRA-p38α^{T180V} complex showing the overall structure of the complex. MKK6^{DD}GRA-p38α^{T180V} is represented as a cartoon and coloured according to (A), AMP-CP nucleotides are represented as balls and sticks (carbon atoms yellow). The MKK6 linker and A-loop are disordered and respectively shown as a full black line and an orange dashed line. The position of the Y182 residue in the p38α A-loop is indicated by a red sphere.

Fig. 2. Novel interaction interfaces between MKK6 and p38α, distal from the active site. (**A**) Surface representation of the MKK6^{DD}GRA-p38α^{T180V} complex. (**B**) Potential interaction between the N-lobes. (**C**) Interaction between the αG-helix of MKK6 and the hydrophobic pocket of p38α. (**D**) αG-helices of p38α and MKK6 in the sharpened Coulomb potential map (black mesh). (**E**) Sequence alignment of MAPK hydrophobic pockets, MAP2K αG-helices and the p38α substrate ATF2 peptide (Clustal coloring scheme). (**F**) Luciferase reporter assay to monitor the activity of the p38α signalling pathway in HEK293T cells, showing the ability of MKK6^{DD} mutants to activate p38α (statistical analysis in Table S4). (**G**) Important interactions around the hydrophobic patch maintained over the course of the MD simulations (view rotated 180° relative to A), inset shows details of observed interactions and plots of distances during the simulation.

Fig. 3. MKK6 N-terminal extension length and secondary structure define the specificity of p38α activation. (**A**) Top view of a MKK6-p38α model, for illustrative purposes, built from the cryo-EM model in which the N-terminal linker was built and MKK6 KIM was reverted to the WT motif. (**B**) Specificity of the MAP2K/MAPK signaling pathways. (**C**) Sequence alignment of MAP2K N-termini. Secondary structural elements are indicated, from experimental structures in blue, and from AlphaFold2 predictions in orange. (**D**) Luciferase reporter assay to monitor the activity of the p38α signalling pathway in HEK293T cells showing the ability of MKK6^{DD} mutants and chimeras to activate p38α (statistical analysis in Table S5).

Fig. 4. MD simulations show p38α Y182 approaching MKK6 ATP. Frame extracted from one of the unrestrained MD simulations in which p38α Y182 approaches the γ-phosphate of MKK6 ATP at a catalytically competent distance (3.8 Å). The π-cation interaction of R95 with Y182 that further stabilizes Y182 close to ATP is shown in a blue dashed line. The frames where p38α Y182 reaches MKK6 ATP at a catalytically-competent distance in this set of simulations are highlighted in the plot of distances over time (blue).

Fig. 5. Communication between the MKK6 KIM and p38α. (**A**) Top and side views of the complex after the detachment of the KIM and consequent transition of p38α to an inactive-like conformation. (**B**) Superposition of p38α with the inactive p38α crystal structure (PDB 3s3i), $RMSD_{backbone}^{p38\alpha}$ = 3.5 Å. Detail: Top: A-loop that breaks the β-sheet motif, Bottom: DFG motif and K/R53-E71 salt-bridge.

Fig. 6. Molecular dynamics simulations of the MKK6GRA-p38α complex show a rotated conformation of p38α favours T180 phosphorylation. (**A**) Simulation frame in which p38α has rotated around its axis with respect to the cryo-EM structure. (**B**) Detailed view around the KIM. The frames where T180 reaches MKK6 ATP at a catalytically-competent distance in this set of simulations are highlighted in the plot of distances over time (blue). (**C**) Luciferase reporter assay to monitor the activity of the p38α signalling pathway in HEK293T cells showing the ability of $MKK6^{DD}$ mutants to activate p38α (statistical analysis in Table S8).

Fig. S1. Expression, purification and activity of the $MKK6^{DD}$GRA-$p38\alpha^{T180V}$ complex. (**A**) $MKK6^{DD}$GRA and $p38\alpha^{T180V}$ were respectively expressed in *Sf21* and *E. coli*. They were purified by affinity purification (StrepTactin and Ni IMAC respectively), followed by cleavage with 3C protease, and reverse affinity purification. Both proteins were mixed, and the complex was purified with size-exclusion chromatography. (**B-C**) Mass spectrometry (Native ESI-QTOF in (B) and LC-MS/MS in (C)) reveals that the complex is highly active, either with $p38\alpha^{WT}$ (left panel) or with $p38\alpha^{T180V}$ (right panel). In the presence of ATP, several sites on both proteins are phosphorylated, including both T180 and Y182 residues of $p38\alpha^{WT}$ A-loop and Y182 residue of $p38\alpha^{T180V}$ A-loop.

Fig. S2. SAXS Curves for $MKK6^{DD}$GRA + p38α mutant complexes. (**A**) On the left tryptic, in blue, shows the IvsQ, Kratky and P(r) plots for $MKK6^{DD}$GRA + p38α mutants + ADP + AlF_4^- complexes. The complex with $p38\alpha^{T180V}$ mutant is more compact than the one with $p38\alpha^{WT}$ which is more compact than the one with $p38\alpha^{Y182F}$ mutation. On the right tryptic, in green, are the same plots for the $MKK6^{DD}$GRA + p38α mutants + AMP-PCP complexes. The complex with $p38\alpha^{WT}$ has a slightly increased Rg compared to the two mutants ones but all share a similar D_{max}. (**B**) χ^2 fits for the cryo-EM $MKK6^{DD}$GRA + $p38\alpha^{T180V}$ model (brick) and MD MKK6 + rotated $p38\alpha^{WT}$ model (salmon).

Fig. S3. Cryo-EM processing and data assessment of the $MKK6^{DD}$GRA-$p38\alpha^{T180V}$ model. (**A**) Exemplary workflow processing for one of the three datasets collected (dataset 2). Data processing was performed in cryoSPARC. A representative micrograph, typical result from heterogeneous refinement, final map with angular sampling and gold-standard Fourier Shell Correlation are also shown. (**B**) Cryo-EM processing of the final particle selection from the three merged datasets to obtain the final reconstruction at 4.0 Å resolution. The final sharpened map, coloured according to local resolution, angular sampling and gold-standard Fourier Shell Correlation are also shown. Representative 2D classes, which yielded the final map, are also shown. (**C**) Fitting of the model into the cryo-EM map. The $MKK6^{DD}$GRA-$p38\alpha^{T180V}$ complex is shown in cartoon representation with α-helices as cylinders, and the sharpened map is shown as a black mesh.

Fig. S4. Comparison of MKK6 crystal structures with the cryo-EM model. Overlay of the cryo-EM structure of $MKK6^{DD}$GRA with (**A**) the structure of MKK6 in an inactive conformation with AMP-PNP bound, (**B**) the structure of MKK6 in an inactive conformation inhibited with staurosporin, (**C**) the structure of MKK6 in an auto-inhibitory dimer, and (**D**) the active structure of MKK7.

Fig. S5. Detailed views of the MKK6^{DD}GRA-p38α^{T180V} model with the sharpened Coulomb potential map. Structural elements of the model are shown in cartoon and stick representation and the sharpened map is shown as a black mesh.

Fig. S6. Interaction and variability of the p38α hydrophobic pocket. The p38α surface is coloured according to hydrophobicity. (**A**) Cryo-EM MKK6^{DD}GRA-p38α^{T180V} model (**B**) Crystal structure of p38α bound to substrate ATF2 peptide showing a similar binding mode as the MKK6 αG helix. (**C-E**) The p38α hydrophobic pocket is flexible: it is opened in inactive p38α crystal structures and closes in active p38α conformation (**F-I**) The p38α hydrophobic pocket can bind small molecules and regulatory lipids: (**F**) β-octyl-D-glucopyranoside (β-OG) detergent, (**G**) phosphatidylinositol ether lipid analogue 24 (PIA24), (**H**) LiPoLis ligand 9l, and (**I**) a fluorinated-pyridine derivative.

Fig. S7. Schematic representation of the phosphorylation mechanism derived from the MD simulations. Although both p38α T180 and Y182 can reach MKK6 ATP at a catalytically competent distance, p38α seems to have to rotate for T180 to reach ATP in most replicas. The difference in experimentally derived kinetic rates measured for the first phosphorylation step may reflect the rotation of p38α N-lobe around its axis that seems to be involved in the T180 phosphorylation only.

Fig. S8. Cellular reporter assay. HEK293T cells are transiently transfected with MKK6^{DD} mutants (orange) and p38α (teal), together with a plasmid encoding firefly luciferase (green) under the control of the AP-1 promoter (purple). When p38α is activated, it phosphorylates several substrates, including ATF2, that will in turn stimulate the AP-1 promoter and trigger the expression of luciferase. Activity of p38α can be directly monitored by measurement of luminescence.

Fig. S9. Important interactions that maintain the KIM of MKK6 in contact with p38α over the course of the MD simulations. The rolling average of the timeseries of side-chain-to-side-chain interactions are shown in black, while the side-chain-to-backbone interactions are shown in green. The reported timeseries refer to one of the simulations with the MKK6 WT sequence (Table S6), however, the same pattern of interactions is observed in three out of the five independent replicas where p38α stays in contact with MKK6.

Movie S1. Detailed presentation of the fitting of the MKK6^{DD}GRA-p38α^{T180V} model in the cryo-EM map and general overview of the model.

Movie S2. Close up view of the interaction between the αG-helices of p38α and MKK6 in the sharpened Coulomb potential map (black mesh).

Movie S3. MD simulation trajectory (1 μs long, unrestrained) where the N-lobe of p38α rotates to allow access of T180 to the ATP bound to MKK6.

References and Notes

1. B. Canovas, A. R. Nebreda. "Diversity and versatility of p38 kinase signalling in health and disease", *Nat Rev Mol Cell Biol* **22**, 346 (2021).10.1038/s41580-020-00322-w
2. M. Bouhaddou *et al.* "The Global Phosphorylation Landscape of SARS-CoV-2 Infection", *Cell* **182**, 685 (2020).10.1016/j.cell.2020.06.034
3. Daniella S. Battagello *et al.* "Unpuzzling COVID-19: tissue-related signaling pathways associated with SARS-CoV-2 infection and transmission", *Clinical Science* **134**, 2137 (2020).10.1042/cs20200904
4. S. Bellon, M. J. Fitzgibbon, T. Fox, H.-M. Hsiao, K. P. Wilson. "The structure of phosphorylated P38γ is monomeric and reveals a conserved activation-loop conformation", *Structure* **7**, 1057 (1999).https://doi.org/10.1016/S0969-2126(99)80173-7
5. S. S. Taylor, A. P. Kornev. "Protein kinases: evolution of dynamic regulatory proteins", *Trends in Biochemical Sciences* **36**, 65 (2011).https://doi.org/10.1016/j.tibs.2010.09.006
6. N. Bluthgen *et al.* "Effects of sequestration on signal transduction cascades", *FEBS J* **273**, 895 (2006).10.1111/j.1742-4658.2006.05105.x
7. F. Ortega, L. Acerenza, H. V. Westerhoff, F. Mas, M. Cascante. "Product dependence and bifunctionality compromise the ultrasensitivity of signal transduction cascades", *Proc Natl Acad Sci U S A* **99**, 1170 (2002).10.1073/pnas.022267399
8. M. Thattai, A. van Oudenaarden. "Attenuation of noise in ultrasensitive signaling cascades", *Biophys J* **82**, 2943 (2002).10.1016/S0006-3495(02)75635-X
9. D. Hammaker, G. S. Firestein. ""Go upstream, young man": lessons learned from the p38 saga", *Annals of the Rheumatic Diseases* **69**, i77 (2010).10.1136/ard.2009.119479
10. K. P. Wilson *et al.* "Crystal structure of p38 mitogen-activated protein kinase", *J Biol Chem* **271**, 27696 (1996).10.1074/jbc.271.44.27696
11. X. Xie *et al.* "Crystal structure of JNK3: a kinase implicated in neuronal apoptosis", *Structure* **6**, 983 (1998).10.1016/S0969-2126(98)00100-2
12. F. Zhang, A. Strand, D. Robbins, M. H. Cobb, E. J. Goldsmith. "Atomic structure of the MAP kinase ERK2 at 2.3 Å resolution", *Nature* **367**, 704 (1994).10.1038/367704a0
13. X. Min *et al.* "The structure of the MAP2K MEK6 reveals an autoinhibitory dimer", *Structure* **17**, 96 (2009).10.1016/j.str.2008.11.007
14. T. Matsumoto *et al.* "Crystal structure of non-phosphorylated MAP2K6 in a putative auto-inhibition state", *J Biochem* **151**, 541 (2012).10.1093/jb/mvs023
15. J. F. Ohren *et al.* "Structures of human MAP kinase kinase 1 (MEK1) and MEK2 describe novel noncompetitive kinase inhibition", *Nat Struct Mol Biol* **11**, 1192 (2004).10.1038/nsmb859
16. M. Schroder *et al.* "Catalytic Domain Plasticity of MKK7 Reveals Structural Mechanisms of Allosteric Activation and Diverse Targeting Opportunities", *Cell Chem Biol* **27**, 1285 (2020).10.1016/j.chembiol.2020.07.014
17. Á. Garai *et al.* "Specificity of Linear Motifs That Bind to a Common Mitogen-Activated Protein Kinase Docking Groove", *Science Signaling* **5**, ra74 (2012).doi:10.1126/scisignal.2003004
18. T. Tanoue, M. Adachi, T. Moriguchi, E. Nishida. "A conserved docking motif in MAP kinases common to substrates, activators and regulators", *Nature Cell Biology* **2**, 110 (2000).10.1038/35000065
19. W. Peti, R. Page. "Molecular basis of MAP kinase regulation", *Protein Science* **22**, 1698 (2013).https://doi.org/10.1002/pro.2374
20. A. Zeke *et al.* "Systematic discovery of linear binding motifs targeting an ancient protein interaction surface on MAP kinases", *Mol Syst Biol* **11**, 837 (2015).10.15252/msb.20156269

21. T. Zhou, L. Sun, J. Humphreys, E. J. Goldsmith. "Docking interactions induce exposure of activation loop in the MAP kinase ERK2", *Structure* **14**, 1011 (2006).10.1016/j.str.2006.04.006
22. C. I. Chang, B. E. Xu, R. Akella, M. H. Cobb, E. J. Goldsmith. "Crystal structures of MAP kinase p38 complexed to the docking sites on its nuclear substrate MEF2A and activator MKK3b", *Mol Cell* **9**, 1241 (2002).10.1016/s1097-2765(02)00525-7
23. M. Dyla, M. Kjaergaard. "Intrinsically disordered linkers control tethered kinases via effective concentration", *Proc Natl Acad Sci U S A* **117**, 21413 (2020).10.1073/pnas.2006382117
24. J. Beenstock, N. Mooshayef, D. Engelberg. "How Do Protein Kinases Take a Selfie (Autophosphorylate)?", *Trends in Biochemical Sciences* **41**, 938 (2016).10.1016/j.tibs.2016.08.006
25. E. Park *et al.* "Architecture of autoinhibited and active BRAF-MEK1-14-3-3 complexes", *Nature* **575**, 545 (2019).10.1038/s41586-019-1660-y
26. Y. Kondo *et al.* "Cryo-EM structure of a dimeric B-Raf:14-3-3 complex reveals asymmetry in the active sites of B-Raf kinases", *Science* **366**, 109 (2019).10.1126/science.aay0543
27. D. F. Brennan *et al.* "A Raf-induced allosteric transition of KSR stimulates phosphorylation of MEK", *Nature* **472**, 366 (2011).10.1038/nature09860
28. L. Braun *et al.* "A Toxoplasma dense granule protein, GRA24, modulates the early immune response to infection by promoting a direct and sustained host p38 MAPK activation", *J Exp Med* **210**, 2071 (2013).10.1084/jem.20130103
29. E. Pellegrini *et al.* "Structural Basis for the Subversion of MAP Kinase Signaling by an Intrinsically Disordered Parasite Secreted Agonist", *Structure* **25**, 16 (2017).10.1016/j.str.2016.10.011
30. R. Diskin, D. Engelberg, O. Livnah. "A novel lipid binding site formed by the MAP kinase insert in p38 alpha", *J Mol Biol* **375**, 70 (2008).10.1016/j.jmb.2007.09.002
31. N. Tzarum, Y. Eisenberg-Domovich, J. J. Gills, P. A. Dennis, O. Livnah. "Lipid molecules induce p38alpha activation via a novel molecular switch", *J Mol Biol* **424**, 339 (2012).10.1016/j.jmb.2012.10.007
32. M. Buhrmann, J. Hardick, J. Weisner, L. Quambusch, D. Rauh. "Covalent Lipid Pocket Ligands Targeting p38alpha MAPK Mutants", *Angew Chem Int Ed Engl* **56**, 13232 (2017).10.1002/anie.201706345
33. M. Buhrmann *et al.* "Structure-based design, synthesis and crystallization of 2-arylquinazolines as lipid pocket ligands of p38alpha MAPK", *PLoS One* **12**, e0184627 (2017).10.1371/journal.pone.0184627
34. K. M. Comess *et al.* "Discovery and characterization of non-ATP site inhibitors of the mitogen activated protein (MAP) kinases", *ACS Chem Biol* **6**, 234 (2011).10.1021/cb1002619
35. O. Laufkotter, H. Hu, F. Miljkovic, J. Bajorath. "Structure- and Similarity-Based Survey of Allosteric Kinase Inhibitors, Activators, and Closely Related Compounds", *J Med Chem* **65**, 922 (2022).10.1021/acs.jmedchem.0c02076
36. X. H. Zhang *et al.* "Targeting the non-ATP-binding pocket of the MAP kinase p38γ mediates a novel mechanism of cytotoxicity in cutaneous T-cell lymphoma (CTCL)", *FEBS Letters* **595**, 2570 (2021).https://doi.org/10.1002/1873-3468.14186
37. K. Kirsch *et al.* "Co-regulation of the transcription controlling ATF2 phosphoswitch by JNK and p38", *Nat Commun* **11**, 5769 (2020).10.1038/s41467-020-19582-3
38. X. Liu *et al.* "A conserved motif in JNK/p38-specific MAPK phosphatases as a determinant for JNK1 recognition and inactivation", *Nat Commun* **7**, 10879 (2016).10.1038/ncomms10879
39. S. A. Foster *et al.* "Activation Mechanism of Oncogenic Deletion Mutations in BRAF, EGFR, and HER2", *Cancer Cell* **29**, 477 (2016).https://doi.org/10.1016/j.ccell.2016.02.010
40. B. Zhang *et al.* "Oncogenic mutations within the β3-αC loop of EGFR/ERBB2/BRAF/MAP2K1 predict response to therapies", *Mol Genet Genomic Med* **8**, e1395 (2020).10.1002/mgg3.1395

41. Y. FLEMING *et al.* "Synergistic activation of stress-activated protein kinase 1/c-Jun N-terminal kinase (SAPK1/JNK) isoforms by mitogen-activated protein kinase kinase 4 (MKK4) and MKK7", *Biochemical Journal* **352**, 145 (2000).10.1042/bj3520145
42. C. Tournier, A. J. Whitmarsh, J. Cavanagh, T. Barrett, R. J. Davis. "The *MKK7* Gene Encodes a Group of c-Jun NH_2-Terminal Kinase Kinases", *Molecular and Cellular Biology* **19**, 1569 (1999).doi:10.1128/MCB.19.2.1569
43. T. O. Fischmann *et al.* "Crystal structures of MEK1 binary and ternary complexes with nucleotides and inhibitors", *Biochemistry* **48**, 2661 (2009).10.1021/bi801898e
44. V. Modi, R. L. Dunbrack. "A Structurally-Validated Multiple Sequence Alignment of 497 Human Protein Kinase Domains", *Scientific Reports* **9**, 19790 (2019).10.1038/s41598-019-56499-4
45. J. Jumper *et al.* "Highly accurate protein structure prediction with AlphaFold", *Nature* **596**, 583 (2021).10.1038/s41586-021-03819-2
46. A. Perez-Gallegos, M. Garcia-Viloca, A. Gonzalez-Lafont, J. M. Lluch. "A QM/MM study of Kemptide phosphorylation catalyzed by protein kinase A. The role of Asp166 as a general acid/base catalyst", *Phys Chem Chem Phys* **17**, 3497 (2015).10.1039/c4cp03579h
47. A. Kuzmanic *et al.* "Changes in the free-energy landscape of p38alpha MAP kinase through its canonical activation and binding events as studied by enhanced molecular dynamics simulations", *Elife* **6** (2017).10.7554/eLife.22175
48. G. S. Kumar, R. Page, W. Peti. "The interaction of p38 with its upstream kinase MKK6", *Protein Science* **30**, 908 (2021).https://doi.org/10.1002/pro.4039
49. Y. Y. Zhang, J. W. Wu, Z. X. Wang. "A distinct interaction mode revealed by the crystal structure of the kinase p38α with the MAPK binding domain of the phosphatase MKP5", *Sci Signal* **4**, ra88 (2011).10.1126/scisignal.2002241
50. C. Dominguez, D. A. Powers, N. Tamayo. "p38 MAP kinase inhibitors: many are made, but few are chosen", *Curr Opin Drug Discov Devel* **8**, 421 (2005)
51. Y. L. Wang *et al.* "Kinetic and mechanistic studies of p38alpha MAP kinase phosphorylation by MKK6", *FEBS J* **286**, 1030 (2019).10.1111/febs.14762
52. J. M. Humphreys, A. T. Piala, R. Akella, H. He, E. J. Goldsmith. "Precisely Ordered Phosphorylation Reactions in the p38 Mitogen-activated Protein (MAP) Kinase Cascade*", *Journal of Biological Chemistry* **288**, 23322 (2013).https://doi.org/10.1074/jbc.M113.462101
53. K. Aoki, K. Takahashi, K. Kaizu, M. Matsuda. "A Quantitative Model of ERK MAP Kinase Phosphorylation in Crowded Media", *Scientific Reports* **3**, 1541 (2013).10.1038/srep01541
54. C. Salazar, T. Höfer. "Multisite protein phosphorylation – from molecular mechanisms to kinetic models", *The FEBS Journal* **276**, 3177 (2009).https://doi.org/10.1111/j.1742-4658.2009.07027.x
55. S. K. Albanese *et al.* "An Open Library of Human Kinase Domain Constructs for Automated Bacterial Expression", *Biochemistry* **57**, 4675 (2018).10.1021/acs.biochem.7b01081
56. Y. Nie, I. Bellon-Echeverria, S. Trowitzsch, C. Bieniossek, I. Berger. "Multiprotein complex production in insect cells by using polyproteins", *Methods Mol Biol* **1091**, 131 (2014).10.1007/978-1-62703-691-7_8
57. M. D. Tully, N. Tarbouriech, R. P. Rambo, S. Hutin. "Analysis of SEC-SAXS data via EFA deconvolution and Scatter", *J Vis Exp* (2021).10.3791/61578
58. D. Schneidman-Duhovny, M. Hammel, J. A. Tainer, A. Sali. "Accurate SAXS profile computation and its assessment by contrast variation experiments", *Biophys J* **105**, 962 (2013).10.1016/j.bpj.2013.07.020
59. M. Schorb, I. Haberbosch, W. J. H. Hagen, Y. Schwab, D. N. Mastronarde. "Software tools for automated transmission electron microscopy", *Nat Methods* **16**, 471 (2019).10.1038/s41592-019-0396-9

60. A. Punjani, J. L. Rubinstein, D. J. Fleet, M. A. Brubaker. "cryoSPARC: algorithms for rapid unsupervised cryo-EM structure determination", *Nat Methods* **14**, 290 (2017).10.1038/nmeth.4169
61. T. Bepler *et al.* "Positive-unlabeled convolutional neural networks for particle picking in cryo-electron micrographs", *Nat Methods* **16**, 1153 (2019).10.1038/s41592-019-0575-8
62. A. J. Jakobi, M. Wilmanns, C. Sachse. "Model-based local density sharpening of cryo-EM maps", *eLife* **6**, e27131 (2017).10.7554/eLife.27131
63. A. Waterhouse *et al.* "SWISS-MODEL: homology modelling of protein structures and complexes", *Nucleic Acids Res* **46**, W296 (2018).10.1093/nar/gky427
64. P. V. Afonine *et al.* "Real-space refinement in PHENIX for cryo-EM and crystallography", *Acta Crystallogr D Struct Biol* **74**, 531 (2018).10.1107/S2059798318006551
65. P. Emsley, K. Cowtan. "Coot: model-building tools for molecular graphics", *Acta Crystallogr D Biol Crystallogr* **60**, 2126 (2004).10.1107/S0907444904019158
66. E. F. Pettersen *et al.* "UCSF ChimeraX: Structure visualization for researchers, educators, and developers", *Protein Sci* **30**, 70 (2021).10.1002/pro.3943
67. C. S. Hughes *et al.* "Ultrasensitive proteome analysis using paramagnetic bead technology", *Mol Syst Biol* **10**, 757 (2014).10.15252/msb.20145625
68. H. Franken *et al.* "Thermal proteome profiling for unbiased identification of direct and indirect drug targets using multiplexed quantitative mass spectrometry", *Nat Protoc* **10**, 1567 (2015).10.1038/nprot.2015.101
69. R. A. Friesner *et al.* "Extra precision glide: docking and scoring incorporating a model of hydrophobic enclosure for protein-ligand complexes", *J Med Chem* **49**, 6177 (2006).10.1021/jm051256o
70. A. Sali, T. L. Blundell. "Comparative protein modelling by satisfaction of spatial restraints", *J Mol Biol* **234**, 779 (1993).10.1006/jmbi.1993.1626
71. G. Martinez-Rosell, T. Giorgino, G. De Fabritiis. "PlayMolecule ProteinPrepare: A Web Application for Protein Preparation for Molecular Dynamics Simulations", *J Chem Inf Model* **57**, 1511 (2017).10.1021/acs.jcim.7b00190
72. K. L. Meagher, L. T. Redman, H. A. Carlson. "Development of polyphosphate parameters for use with the AMBER force field", *J Comput Chem* **24**, 1016 (2003).10.1002/jcc.10262
73. F. P. Buelens, H. Leonov, B. L. de Groot, H. Grubmuller. "ATP-Magnesium Coordination: Protein Structure-Based Force Field Evaluation and Corrections", *J Chem Theory Comput* **17**, 1922 (2021).10.1021/acs.jctc.0c01205
74. M. J. Abraham *et al.* "GROMACS: High performance molecular simulations through multi-level parallelism from laptops to supercomputers", *SoftwareX* **1-2**, 19 (2015).https://doi.org/10.1016/j.softx.2015.06.001
75. G. A. Tribello, M. Bonomi, D. Branduardi, C. Camilloni, G. Bussi. "PLUMED 2: New feathers for an old bird", *Computer Physics Communications* **185**, 604 (2014).https://doi.org/10.1016/j.cpc.2013.09.018
76. G. Bussi, D. Donadio, M. Parrinello. "Canonical sampling through velocity rescaling", *The Journal of Chemical Physics* **126**, 014101 (2007).10.1063/1.2408420
77. M. Bernetti, G. Bussi. "Pressure control using stochastic cell rescaling", *The Journal of Chemical Physics* **153**, 114107 (2020).10.1063/5.0020514
78. P. consortium. "Promoting transparency and reproducibility in enhanced molecular simulations", *Nat Methods* **16**, 670 (2019).10.1038/s41592-019-0506-8
79. X. Daura *et al.* "Peptide Folding: When Simulation Meets Experiment", *Angewandte Chemie International Edition* **38**, 236 (1999).https://doi.org/10.1002/(SICI)1521-3773(19990115)38:1/2<236::AID-ANIE236>3.0.CO;2-M

80. I. Galdadas *et al.* "Structural basis of the effect of activating mutations on the EGF receptor", *eLife* **10**, e65824 (2021).10.7554/eLife.65824
81. Y. Shan, A. Arkhipov, E. T. Kim, A. C. Pan, D. E. Shaw. "Transitions to catalytically inactive conformations in EGFR kinase", *Proceedings of the National Academy of Sciences* **110**, 7270 (2013).doi:10.1073/pnas.1220843110
82. J. Eswaran *et al.* "Structure of the Human Protein Kinase MPSK1 Reveals an Atypical Activation Loop Architecture", *Structure* **16**, 115 (2008).https://doi.org/10.1016/j.str.2007.10.026

Table S1. Calculated SAXS data using Scatter and FoxS.
* Theoretical Rg using ATSAS

	I(0)	Rg (Å)	MW estimation (kDa)	D_{max} (Å)	χ^2 against cryo-EM MKK6^{DD}GRA + p38α^{T180V} model	χ^2 against MD MKK6 + rotated p38α^{WT} model
MKK6^{DD}GRA + p38α^{WT} + AMP-PCP	3.0E-01	41.6	68	139	136	94.0
MKK6^{DD}GRA + p38α^{T180V} + AMP-PCP	2.3E-01	39.1	77	140	138	96.6
MKK6^{DD}GRA + p38α^{Y182F} + AMP-PCP	3.0E-01	39.4	70	139	165	115
MKK6^{DD}GRA + p38α^{WT} + ADP + AlF_4^-	2.6E-01	32.2	65	121	19.1	10.1
MKK6^{DD}GRA + p38α^{T180V} + ADP + AlF_4^-	2.3E-01	29.6	59	115	5.91	6.46
MKK6^{DD}GRA + p38α^{Y182F} + ADP + AlF_4^-	2.8E-01	35.3	69	134	86.6	55.1
cryo-EM MKK6^{DD}GRA + p38α^{T180V} model		29*				
MD MKK6 + rotated p38α^{WT} model		32*				

Table S2. Summary of cross-correlation scores for the rebuilt model and the predicted structures.

	Entire complex	**Hydrophobic patch**	**KIM domain**	**p38α activation loop**	**MKK6 region close to the linker**
Rebuilt model	0.492	0.441	0.488	0.305	0.248
AF2 model1	0.271	0.152	0.349	0.288	0.272
AF2 model2	0.204	0.190	0.401	0.232	0.010
MODELLER model1	0.477	0.497	0.450	0.307	0.239
MODELLER model2	0.474	0.486	0.427	0.317	0.226
MODELLER model3	0.462	0.478	0.436	0.320	0.140
MODELLER model4	0.486	0.498	0.439	0.322	0.263
MODELLER model5	0.479	0.396	-	0.315	-
Cluster derived from MD simulation*	0.283	0.242	0.351	0.261	0.174

* The highest cross-correlation score is reported.

Table S3. Cryo-EM data collection, processing and refinement

Data collection and processing	**MKK6^{DD}GRA-p38α^{T180V} complex (8A8M)**
Magnification	215,000
Voltage (kV)	300
Electron exposure (e^-/Å^2)	62.77
Defocus range (μm)	-1.5 to -3
Pixel size (Å)	0.638
Final particle images (no.)	35,123
Map resolution (Å)	4.0 Å
FSC threshold	0.143
Map resolution range (Å)	2.7-6.5 (25th to 75th percentile)
Refinement	
Initial models used	5ETA, 5ETC and a homology model of 6YG1
Map sharpening factor (Å^2)	200
Model composition	
Non-hydrogen atoms	5249
Protein residues	5157
Ligands	92
R.M.S deviations	
Bond length (Å)	0.004
Bond angles (°)	0.934
Validation	
MolProbity score	2.44
Clash score	28.69
Poor rotamers (%)	0.52
Ramachandran plot	
Favoured (%)	91.69
Allowed (%)	8.31
Outliers (%)	0

Table S4. Statistical analysis of cellular assay (Fig. 2.)

p38	MKK6	Mean	se	Shapiro Wilk	Welch t test against p38+/MKK6DD	Significance (<0.5 *; <0.01 **; < 0.001 ***)
+	-	2%	0.002	4,36E-01	3,66E-12	***
+	DD	100 %	0.057	7,71E-01	1,00E+00	NS
+	penta Ala	31 %	0.023	7,76E-01	1,68E-10	***
+	T87A V88A N89A	168 %	0.122	8,21E-01	3,57E-04	***

Table S5. Statistical analysis of cellular assay (Fig. 3.)

p38	MKK6	Mean	se	Shapiro Wilk	Welch t test against p38+/MKK6DD	Wilcoxon rank sum exact test against p38+/MKK6DD	Significance (<0.5 *; <0.01 **; < 0.001 ***)
+	-	2 %	0.004	2,47E-01	1,43E-11		***
+	DD	100 %	0.055	1,32E-01	1,00E+00		NS
+	10 Ala insertion	53 %	0.040	3,87E-01	3,47E-07		***
+	10 res deletion	50 %	0.040	1,37E-01	1,22E-07		***
+	20 Ala insertion	62 %	0.052	2,02E-01	4,40E-05		***
+	Ala scan 18-29	73 %	0.054	4,37E-01	2,09E-03		**
+	Ala scan 28-39	101 %	0.078	2,32E-01	8,84E-01		NS
+	Ala scan 38-49	42 %	0.022	4,35E-01	6,15E-09		***
+	MEK1 linker	12 %	0.007	9,16E-01	5,63E-11		***
+	MEK2 linker	14 %	0.017	1,01E-01	1,72E-11		***
+	MKK3 linker	44 %	0.028	6,96E-01	9,74E-09		***
+	MKK3 short linker	44 %	0.035	5,61E-02	9,76E-09		***
+	MKK4 linker	29 %	0.045	1,83E-02		1,96E-06	***
+	MKK4 short linker	16 %	0.017	4,83E-01	2,11E-11		***
+	MKK7 linker	34 %	0.029	2,54E-01	5,77E-10		***
+	MKK7 short linker	26 %	0.037	4,95E-01	6,70E-11		***

Table S6. Summary of the unbiased simulations of the p38α-MKK6.
The reported times correspond to the simulation time of each independent unbiased simulation.
* started from a conformation originating from the restrained simulations of p38α-MKK6GRA, where p38α Y182 was close to MKK6 ATP.

System		Simulation time (ns)	Inter-kinase contacts restraints
p38α-MKK6GRA	rep1	1000	No
	rep2	1000	No
	rep3	1000	No
	rep4	1000	No
	rep5	1000	No
p38α-MKK6GRA	rep1	1000	Yes
	rep2	1000	Yes
	rep3	1000	Yes
	rep4	1000	Yes
	rep5	1000	Yes
p38α-MKK6GRA	rep1	1000	No*
	rep2	1000	No*
	rep3	2000	No*
p38α-MKK6	rep1	1000	No
	rep2	1000	No
	rep3	1000	No
	rep4	1000	No
	rep5	1000	No
Total simulation time		19000	

Table S7. Comparison of MD-derived atom distances (Å) important for the phosphorylation of p38α at T180 and Y182 by MKK6 with atom distances reported for the SP20 phosphoryl transfer mechanism catalysed by the cAMP-dependent protein kinase (PKA). The reported distances for the PKA-SP20 phosphorylation were derived from QM/MM calculations (*46*), while the MD distances where derived from a frame where either T180 or Y182 was the closest to MKK6 ATP.

	QM/MM	MD simulations			
	PKA-SP20	**MKK6GRA-p38α** (rep3 / rep5, no restraints)	**MKK6GRA-p38α** (rep3 / rep4, with restraints)	**MKK6GRA-p38α** (rep3, released restraints)	**MKK6-p38α** (rep2 / rep5, no restraints)
$ATP_{(P\gamma)}$-$T180_{(OH)}$	3.76	3.3 / 16.5	10.4 / 14.4	13.0	13.5 / 5.6
$T180_{(HG1)}$-$ATP_{(OG1)}$	1.81	1.6 / 15.2	11.3 / 13.3	14.0	17.8 / 8.7
$T180_{(HG1)}$-$ATP_{(OG2)}$		2.9 / 17.5	9.1 / 14.8	15.2	15.2 / 8.1
$T180_{(HG1)}$-$ATP_{(OG3)}$		1.7 / 16.1	9.6 / 15.8	12.8	17.0 / 7.8
$ATP_{(P\gamma)}$-$Y182_{(OH)}$	3.76	17.4 / 3.8	4.4 / 3.5	3.6	4.3 /15.1
$Y182_{(HH)}$-$ATP_{(OG1)}$	1.81	17.3 / 1.9	5.0 / 1.4	3.7	7.3 / 19.1
$Y180_{(HH)}$-$ATP_{(OG2)}$		17.5 / 3.8	3.3 / 3.6	4.8	7.5/ 18.3
$Y182_{(HH)}$-$ATP_{(OG3)}$		16.9 / 3.7	2.9 / 3.9	2.6	7.5 / 17.9

Table S8. Statistical analysis of cellular assay (Fig. 4.)

p38	MKK6	Mean	se	Shapiro Wilk	Welch t test against p38+/MKK6DD	Significance (<0.5 *; <0.01 **; < 0.001 ***)
+	-	2%	0.004	5.42E-01	2.65E-09	***
+	DD	100%	0.044	2.76E-01	1.00E+00	NS
+	K17A	126%	0.104	8.85E-02	3.68E-02	*

Table S9. SAXS data collection and analysis

Data-collection parameters	
Instrument:	Diamond light source B21
Wavelength (Å)	0.9524
q-range ($Å^{-1}$)	0.0026-0.34
Sample-to-detector distance (m)	3.7
Concentration (mg/mL)	5
Temperature (K)	277
Detector	Eiger 4M (Dectris)
Flux (photons/s)	$2*10^{12}$
Beam size (µm)	1102*240

Structural parameters (AMP-PCP)	**MKK6^{DD}GRA + p38α^{WT} + AMP-PCP**	**MKK6^{DD}GRA + p38α^{T180V} + AMP-PCP**	**MKK6^{DD}GRA + p38α^{Y182F} + AMP-PCP**
I0 (kDa) [from Guinier]	3,00E-01	2,30E-01	3,00E-01
Rg (Å) [from Guinier]	41,6	39,1	39,4
qminRg - qmaxRg used for Guinier	$1.4*10^{-2}$-$3.1*10^{-2}$	$1.8*10^{-2}$-$3.3*10^{-2}$	$1.6*10^{-2}$-$3.2*10^{-2}$
Volume ($Å^3$)	$1.5*10^5$	$1.5*10^5$	$1.4*10^5$
D_{max} (Å)	139	140	139
Calculated MW	68	77	70

Structural parameters (ADP + AlF_4^-)	**MKK6^{DD}GRA + p38α^{WT} + ADP + AlF_4^-**	**MKK6^{DD}GRA + p38α^{T180V} + ADP + AlF_4^-**	**MKK6^{DD}GRA + p38α^{Y182F} + ADP + AlF_4^-**
I0 (kDa) [from Guinier]	2,60E-01	2,30E-01	2,80E-01
Rg (Å) [from Guinier]	32,2	29,6	35,3
qminRg - qmaxRg used for Guinier	$1.4*10^{-2}$-$4.0*10^{-2}$	$1.7*10^{-2}$-$4.3*10^{-2}$	$1.4*10^{-2}$-$3.6*10^{-2}$
Volume ($Å^3$)	$1.3*10^5$	$1.2*10^5$	$1.4*10^5$
D_{max} (Å)	121	115	134
Calculated MW	65	59	69

Software employed	
Primary data reduction:	B21 autoprocessing pipeline
Data processing	Scatter IV
χ^2 determination	FoXs

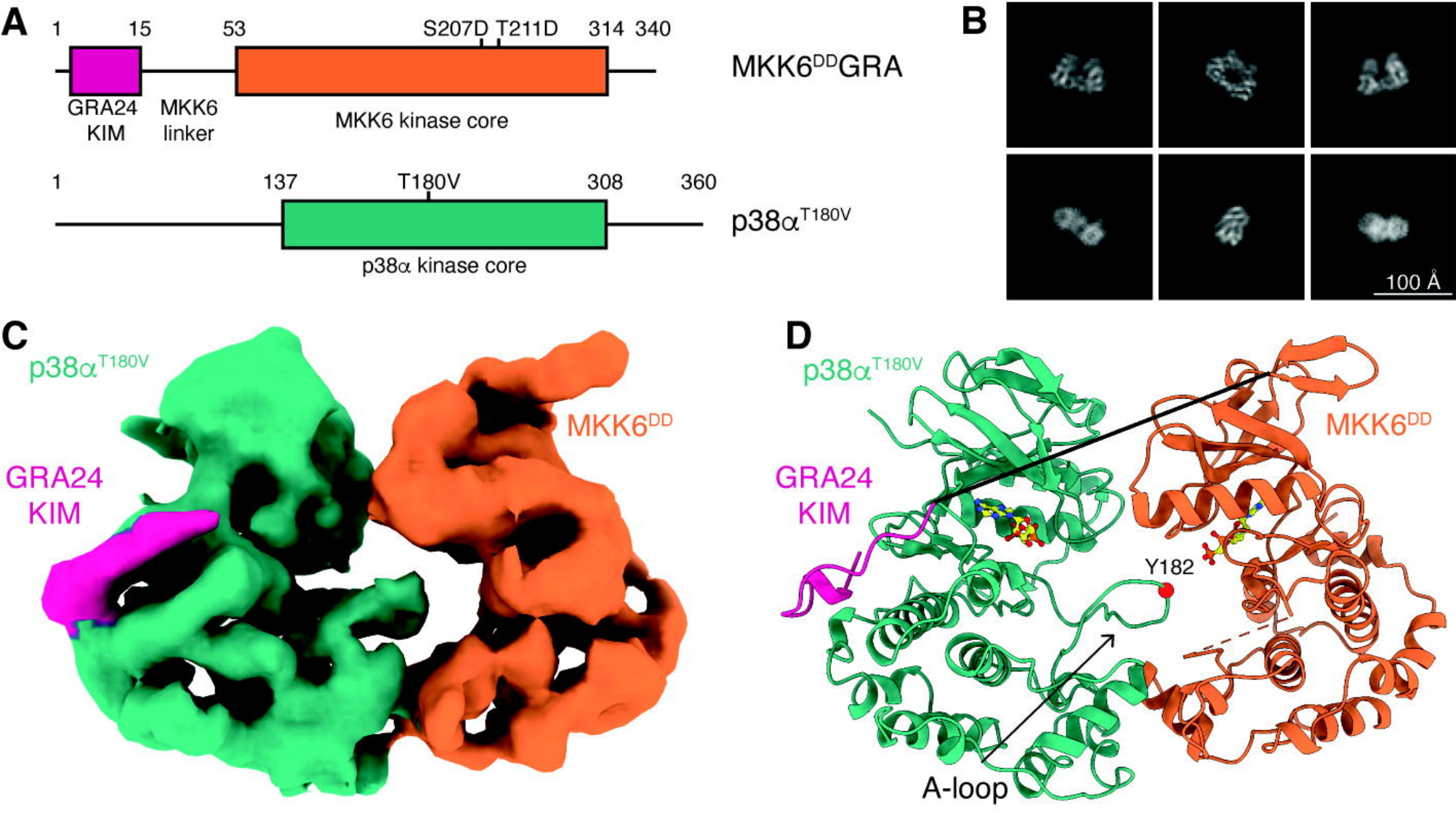
A
1
15
53
S207D T211D
314 340
MKK6DDGRA
GRA24 KIM
MKK6 linker
MKK6 kinase core
1
137
T180V
308
360
p38αT180V
p38α kinase core
B
100 Å
C
p38αT180V
MKK6DD
GRA24 KIM
D
p38αT180V
MKK6DD
GRA24 KIM
Y182
A-loop

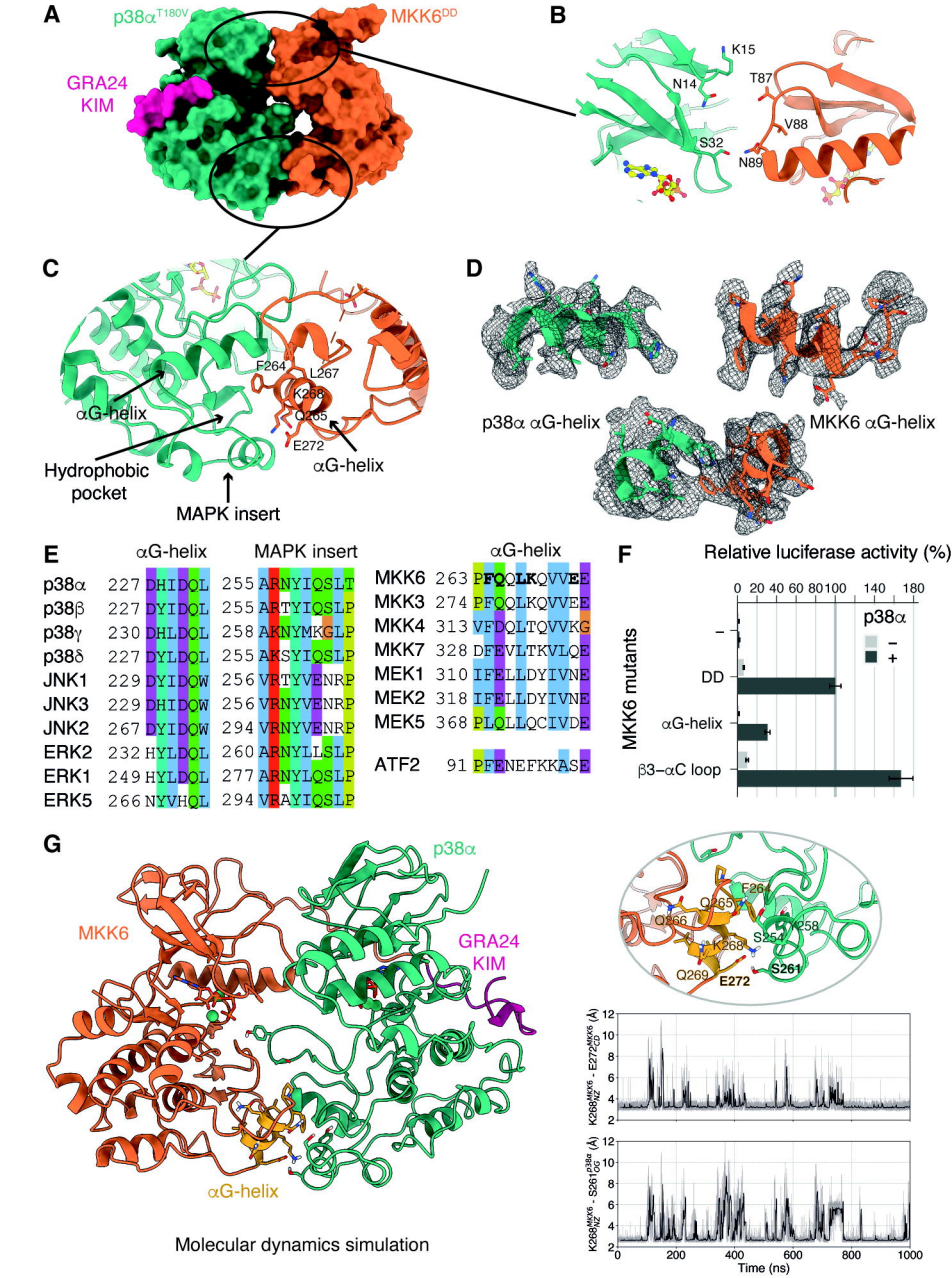
A
p38α T180V
MKK6 DD
GRA24 KIM
B
K15
N14
T87
V88
S32
N89
C
F264
L267
K268
Q265
E272
αG-helix
αG-helix
Hydrophobic pocket
MAPK insert
D
p38α αG-helix
MKK6 αG-helix
E
αG-helix
MAPK insert
αG-helix
p38α 227 DHIDQL 255 ARNYIQSLT
p38β 227 DYIDQL 255 ARTYIQSLP
p38γ 230 DHLDQL 258 AKNYMKGLP
p38δ 227 DYLDQL 255 AKSYIQSLP
JNK1 229 DYIDQW 256 VRTYVENRP
JNK3 229 DHIDQW 256 VRNYVENRP
JNK2 267 DYIDQW 294 VRNYVENRP
ERK2 232 HYLDQL 260 ARNYLLSLP
ERK1 249 HYLDQL 277 ARNYLQSLP
ERK5 266 NYVHQL 294 VRAYIQSLP
MKK6 263 PFQQLKQVVEE
MKK3 274 PFQQLKQVVEE
MKK4 313 VFDQLTQVVKG
MKK7 328 DFEVLTKVLQE
MEK1 310 IFELLDYIVNE
MEK2 318 IFELLDYIVNE
MEK5 368 PLQLLQCIVDE
ATF2 91 PFENEFKKASE
F
Relative luciferase activity (%)
0 20 40 60 80 100 140 180
p38α
–
+
MKK6 mutants
–
DD
αG-helix
β3–αC loop
G
p38α
MKK6
GRA24 KIM
αG-helix
Molecular dynamics simulation
F264
Q265
Q266
K258
S254
K268
S261
Q269
E272
Time (ns)

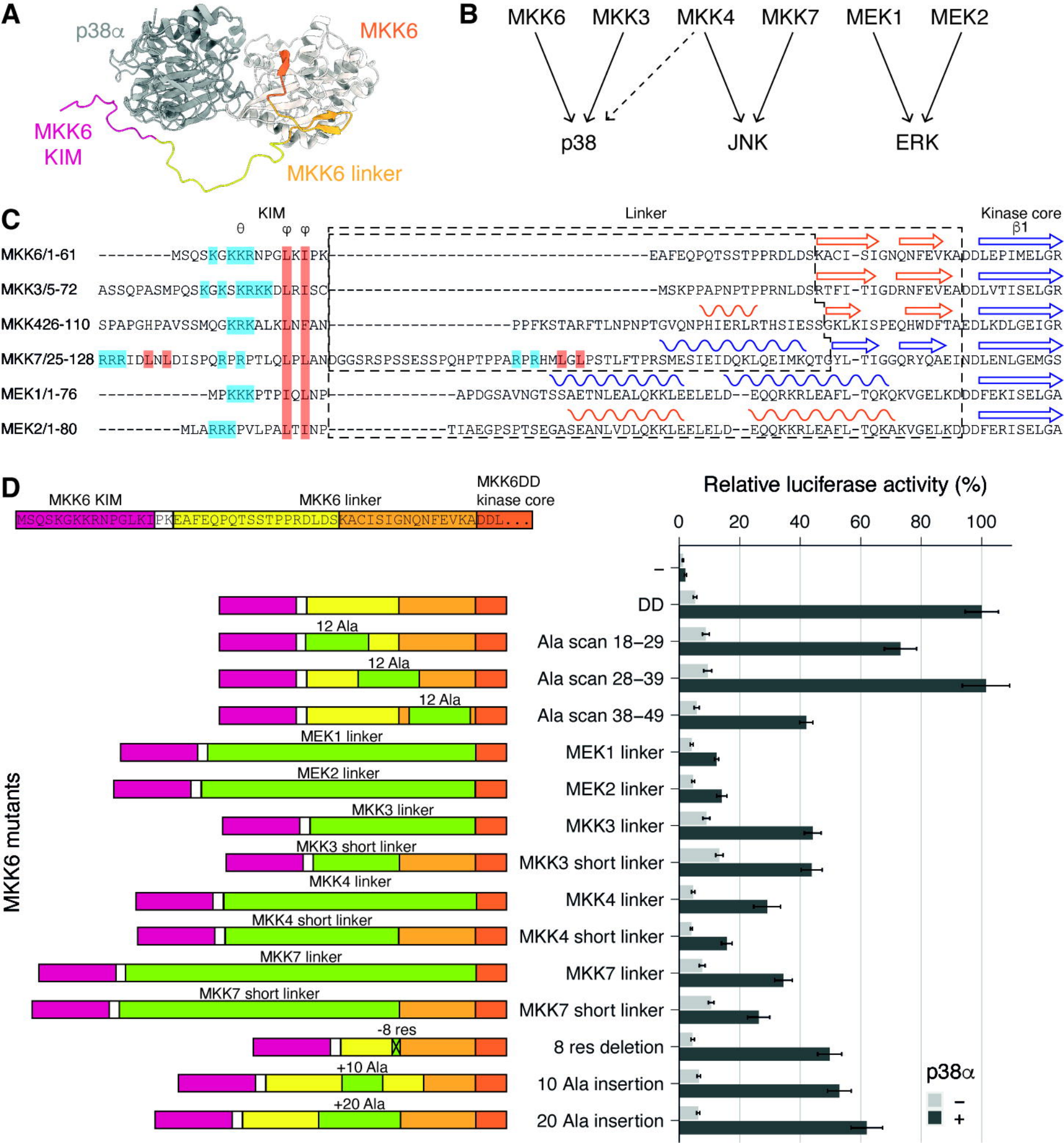
A
p38α
MKK6
MKK6 KIM
MKK6 linker
B
MKK6
MKK3
MKK4
MKK7
MEK1
MEK2
p38
JNK
ERK
C
KIM
Linker
Kinase core
θ
φ φ
β1
MKK6/1-61 --------MSQSKGKKRNPGLKIPK----------EAFEQPQTSSTPPRDLDSKACI-SIGNQNFEVKADDLEPIMELGR
MKK3/5-72 ASSQPASMPQSKGKSKRKKDLRISC----------MSKPPAPNPTPPRNLDSRTFI-TIGDRNFEVEADDLVTISELGR
MKK426-110 SPAPGHPAVSSMQGKRKALKLNFAN----------PPFKSTARFTLNPNPTGVQNPHIERLRTHSIESSGKLKISPEQHWDFTAEDLKDLGEIGR
MKK7/25-128 RRRIDLNLDISPQRPRPTLQLPLANDGGSRSPSSESSPQHPTPPARPRHMLGLPSTLFTPRSMESIEIDQKLQEIMKQTGYL-TIGGQRYQAEINDLENLGEMGS
MEK1/1-76 ----------MPKKKPTPIQLNP----------APDGSAVNGTSSAETNLEALQKKLEELELD--EQQRKRLEAFL-TQKQKVGELKDDDFEKISELGA
MEK2/1-80 ---------MLARRKPVLPALTINP----------TIAEGPSPTSEGASEANLVDLQKKLEELELD--EQQKKRLEAFL-TQKAKVGELKDDDFERISELGA
D
MKK6 KIM
MKK6 linker
MKK6DD kinase core
MSQSKGKKRNPGLKIPKEAFEQPQTSSTPPRDLDSKACISIGNQNFEVKADDL...
MKK6 mutants
12 Ala
12 Ala
12 Ala
MEK1 linker
MEK2 linker
MKK3 linker
MKK3 short linker
MKK4 linker
MKK4 short linker
MKK7 linker
MKK7 short linker
-8 res
+10 Ala
+20 Ala
Relative luciferase activity (%)
0
20
40
60
80
100
–
DD
Ala scan 18–29
Ala scan 28–39
Ala scan 38–49
MEK1 linker
MEK2 linker
MKK3 linker
MKK3 short linker
MKK4 linker
MKK4 short linker
MKK7 linker
MKK7 short linker
8 res deletion
10 Ala insertion
20 Ala insertion
p38α
–
+

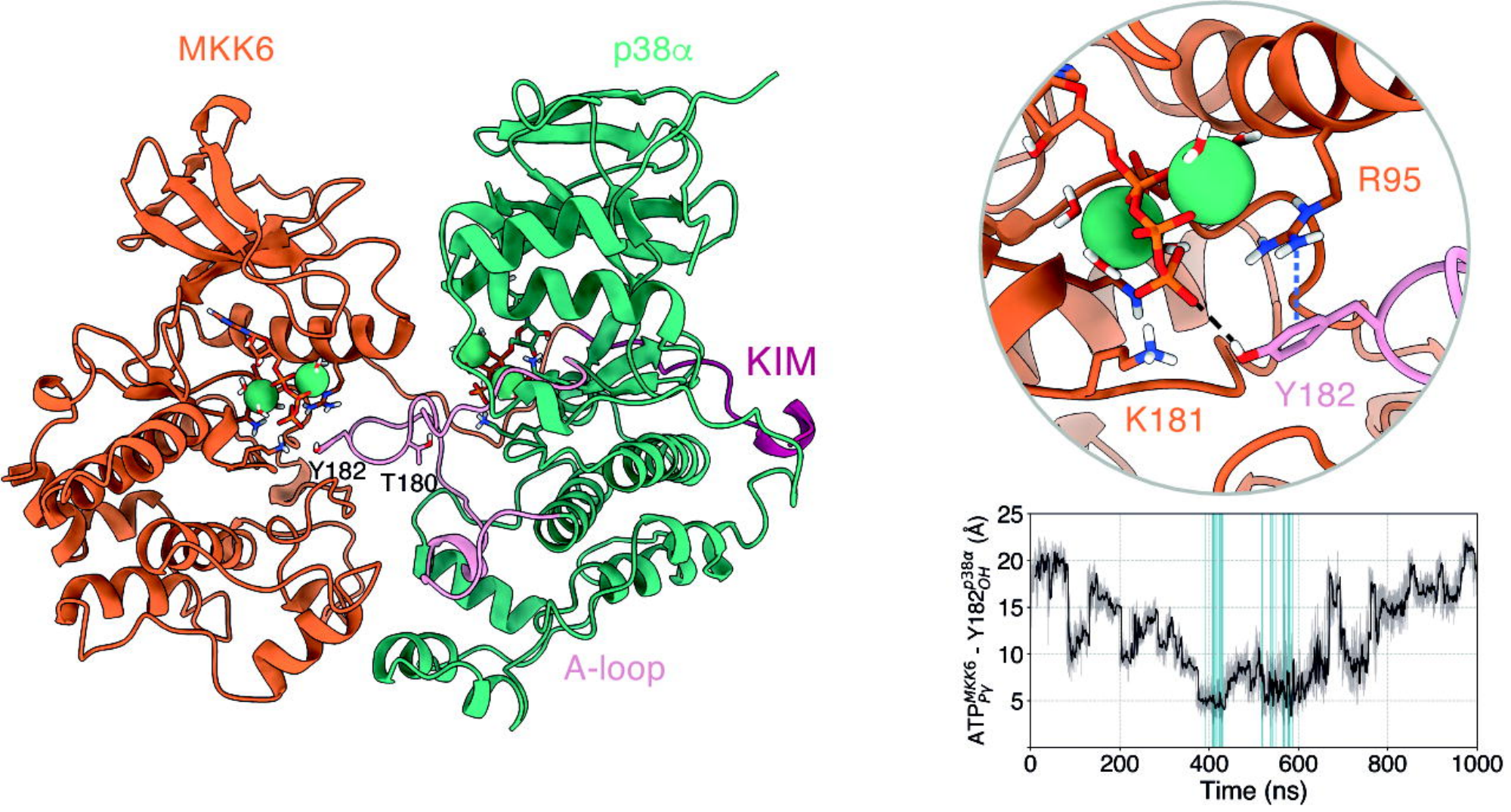
MKK6
p38α
KIM
Y182
T180
A-loop
R95
K181
Y182
25
20
15
10
5
0
200
400
600
800
1000
Time (ns)
$ATP_{P\gamma}^{MKK6}$ - $Y182_{OH}^{p38\alpha}$ (Å)

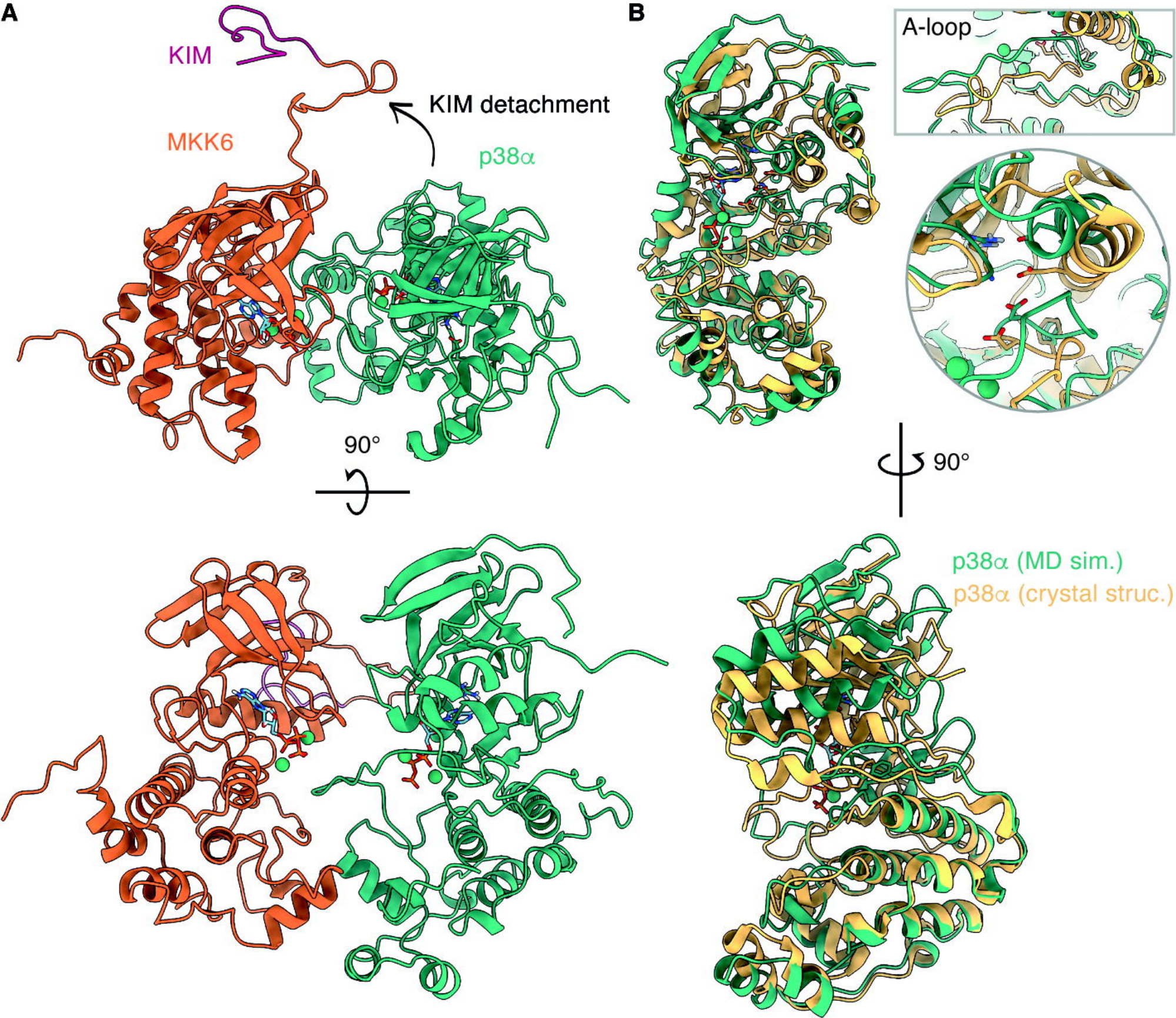
A
KIM
KIM detachment
MKK6
p38α
90°
B
A-loop
90°
p38α (MD sim.)
p38α (crystal struc.)

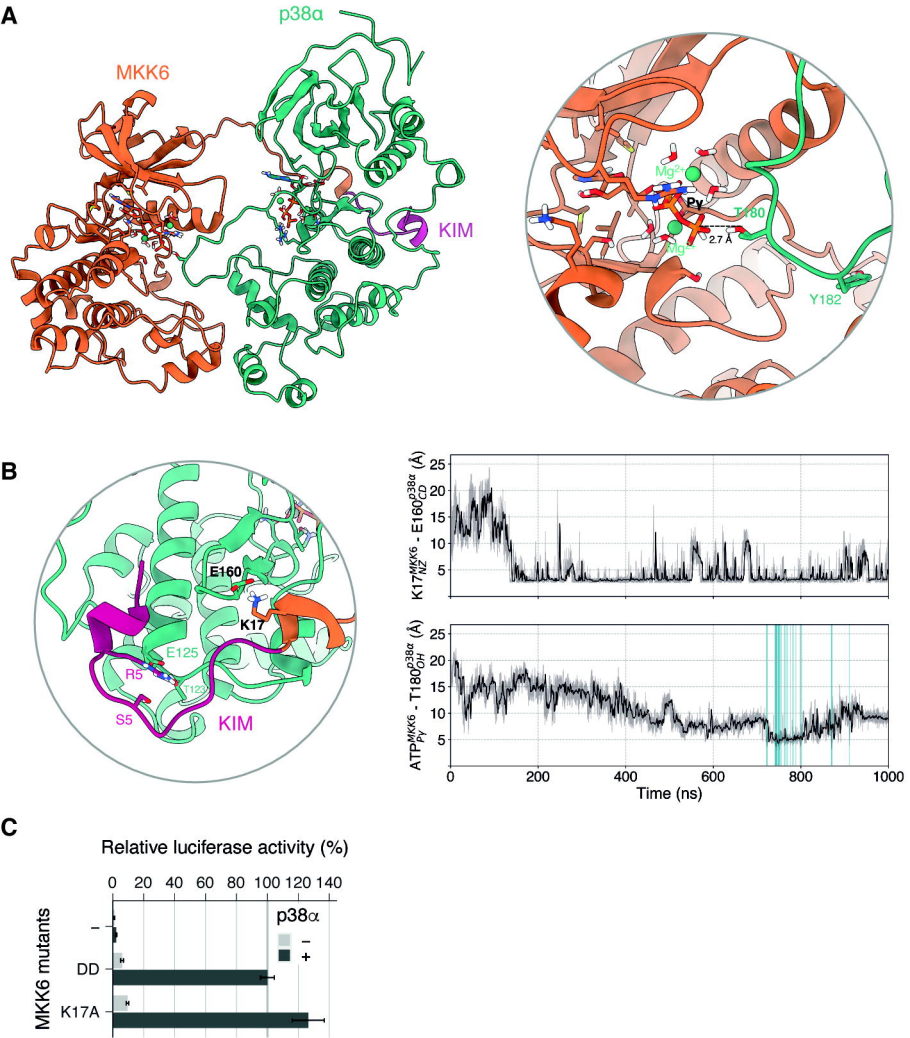
A
p38α
MKK6
KIM
Mg++
Py
T180
2.7 Å
Mg
Y182
B
E160
K17
E125
R5
T123
S5
KIM
K17NZMKK6 - E160CDp38α (Å)
ATPPyMKK6 - T180OHp38α (Å)
Time (ns)
C
Relative luciferase activity (%)
p38α
–
+
MKK6 mutants
–
DD
K17A

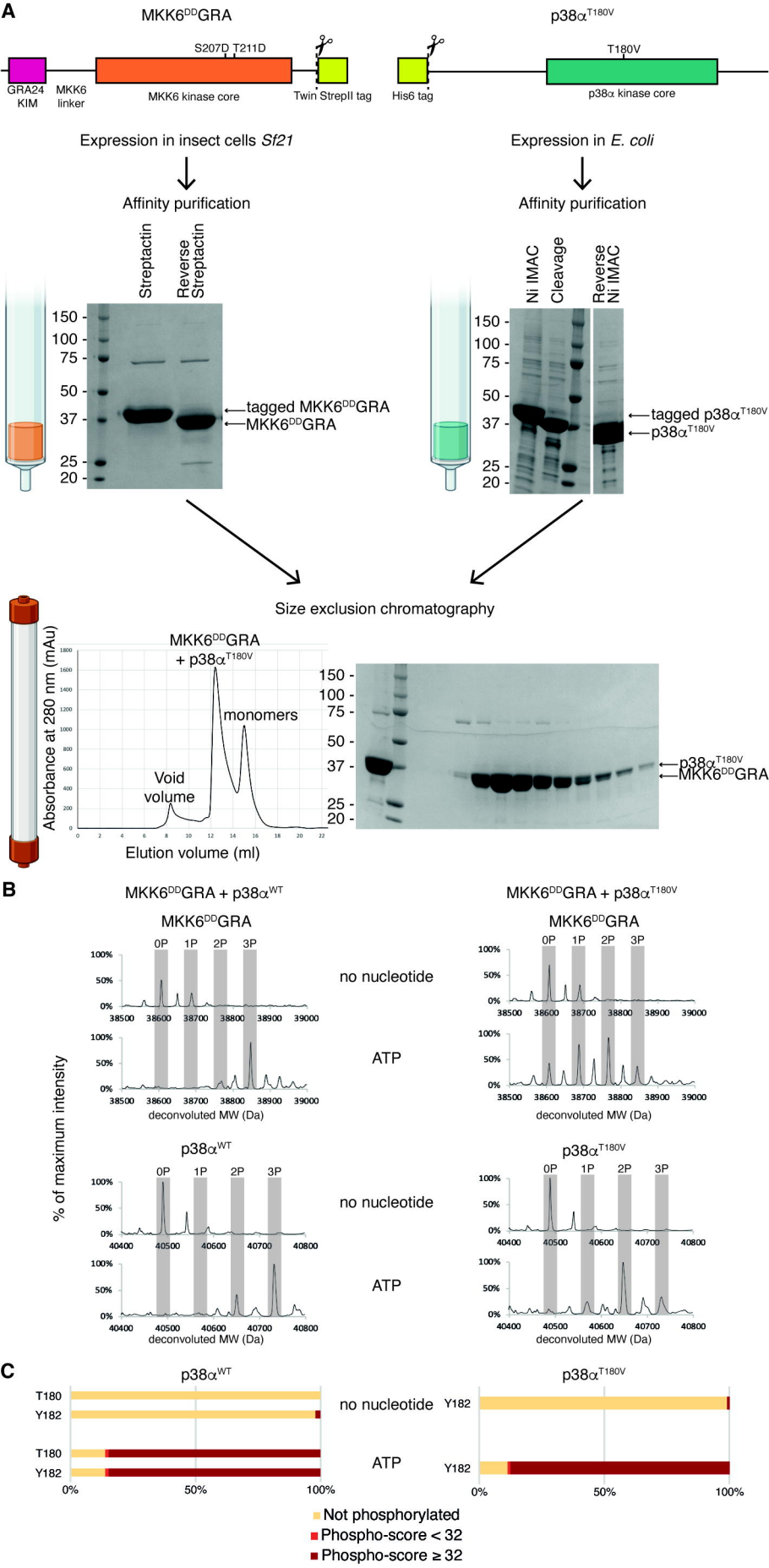
A
MKK6DDGRA
S207D T211D
GRA24 KIM
MKK6 linker
MKK6 kinase core
Twin StrepII tag
p38αT180V
T180V
His6 tag
p38α kinase core
Expression in insect cells Sf21
Expression in E. coli
Affinity purification
Affinity purification
Streptactin
Reverse Streptactin
Ni IMAC
Cleavage
Reverse Ni IMAC
150
100
75
50
37
25
20
tagged MKK6DDGRA
MKK6DDGRA
tagged p38αT180V
p38αT180V
Size exclusion chromatography
MKK6DDGRA + p38αT180V
monomers
Void volume
Absorbance at 280 nm (mAu)
Elution volume (ml)
p38αT180V
MKK6DDGRA
B
MKK6DDGRA + p38αWT
MKK6DDGRA + p38αT180V
MKK6DDGRA
0P 1P 2P 3P
no nucleotide
ATP
deconvoluted MW (Da)
% of maximum intensity
p38αWT
p38αT180V
C
T180
Y182
Not phosphorylated
Phospho-score < 32
Phospho-score ≥ 32

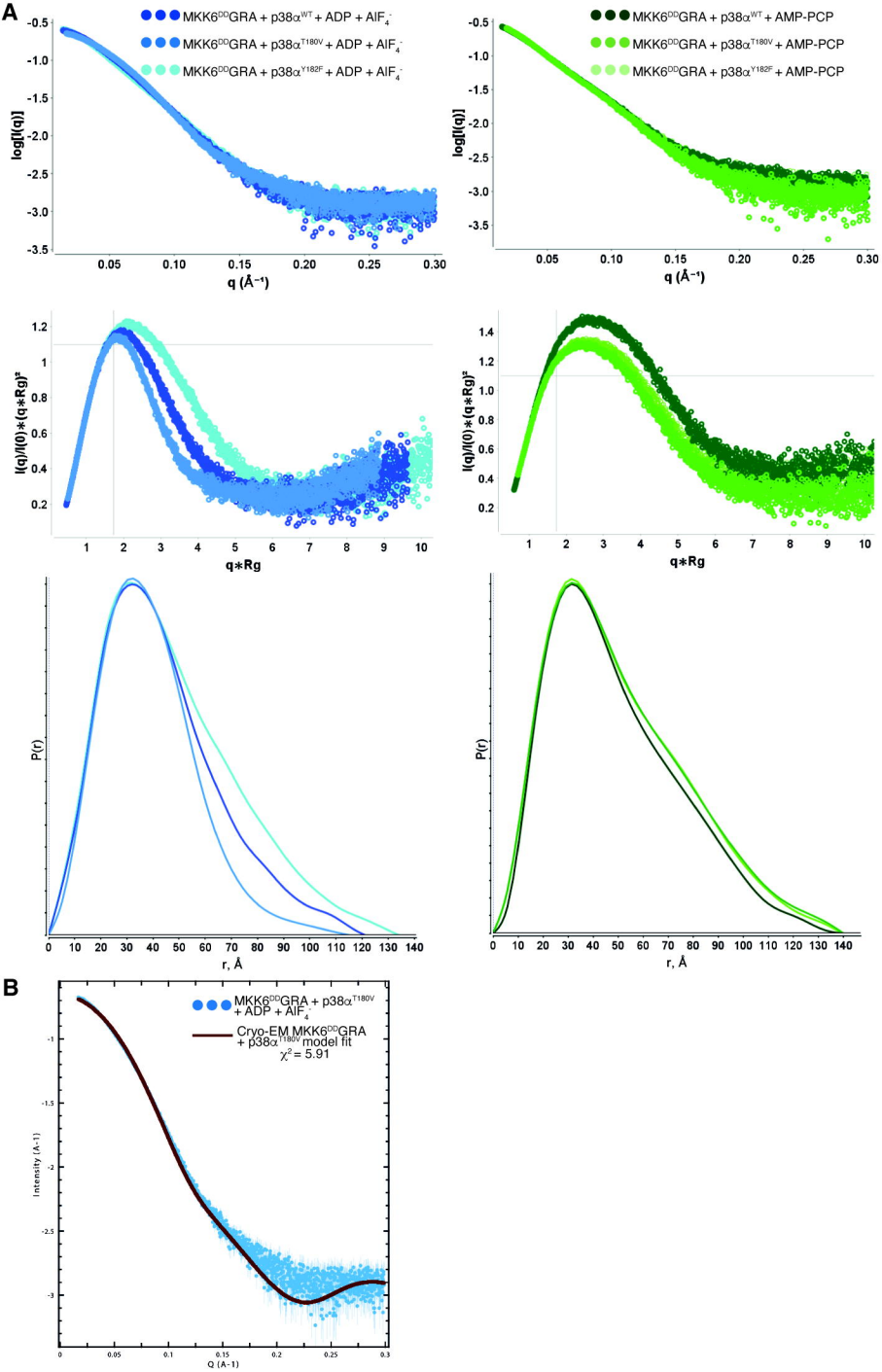
A
MKK6DDGRA + p38αWT + ADP + AlF4-
MKK6DDGRA + p38αT180V + ADP + AlF4-
MKK6DDGRA + p38αY182F + ADP + AlF4-
log[I(q)]
q (Å⁻¹)
MKK6DDGRA + p38αWT + AMP-PCP
MKK6DDGRA + p38αT180V + AMP-PCP
MKK6DDGRA + p38αY182F + AMP-PCP
I(q)/I(0)*(q*Rg)²
q*Rg
P(r)
r, Å
B
MKK6DDGRA + p38αT180V + ADP + AlF4-
Cryo-EM MKK6DDGRA + p38αT180V model fit
χ² = 5.91
Intensity (A-1)
Q (A-1)

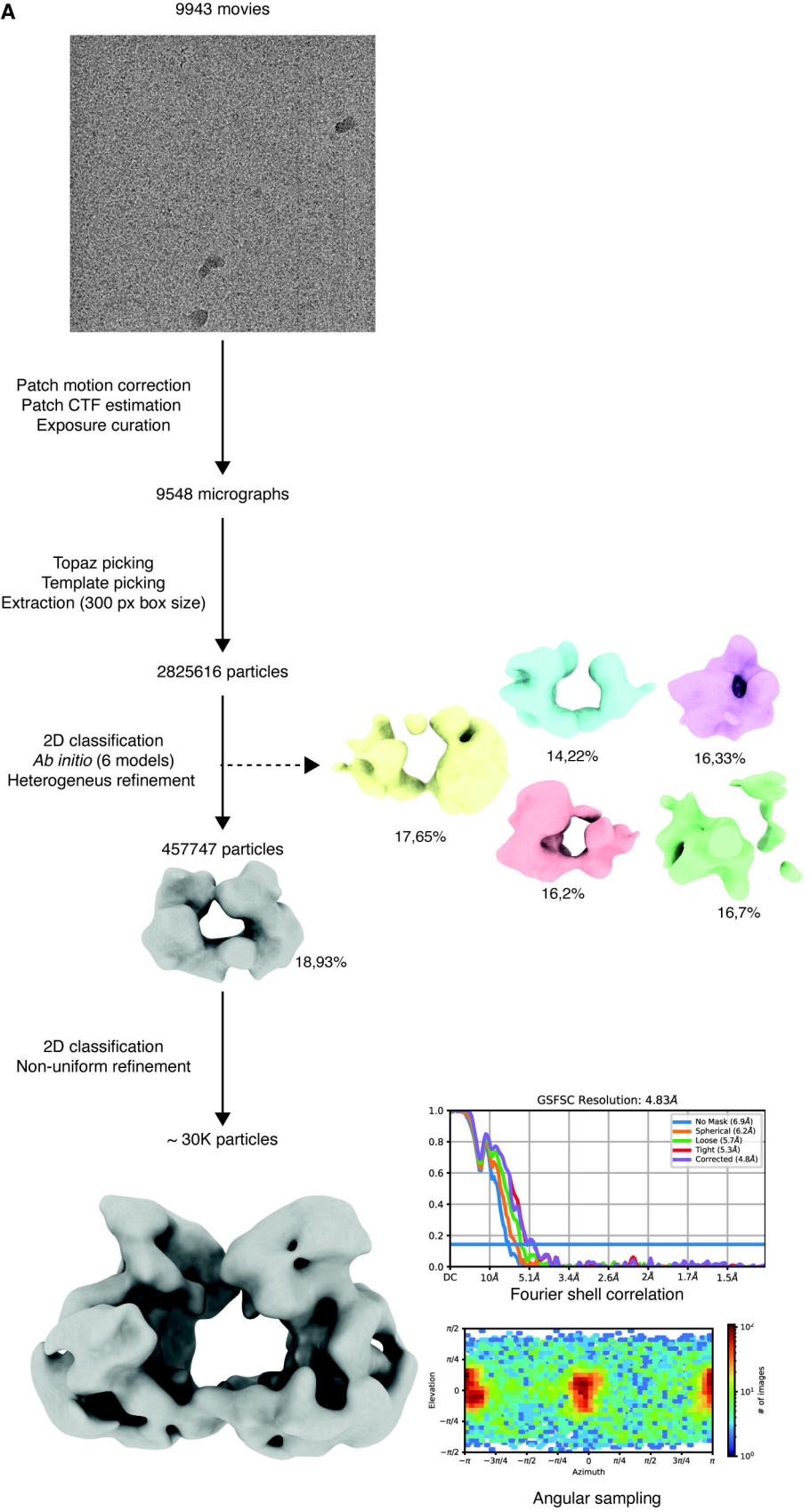
A
9943 movies
Patch motion correction
Patch CTF estimation
Exposure curation
9548 micrographs
Topaz picking
Template picking
Extraction (300 px box size)
2825616 particles
2D classification
Ab initio (6 models)
Heterogeneus refinement
17,65%
14,22%
16,33%
16,2%
16,7%
457747 particles
18,93%
2D classification
Non-uniform refinement
~ 30K particles
GSFSC Resolution: 4.83Å
No Mask (6.9Å)
Spherical (6.2Å)
Loose (5.7Å)
Tight (5.3Å)
Corrected (4.8Å)
Fourier shell correlation
Elevation
Azimuth
# of images
Angular sampling

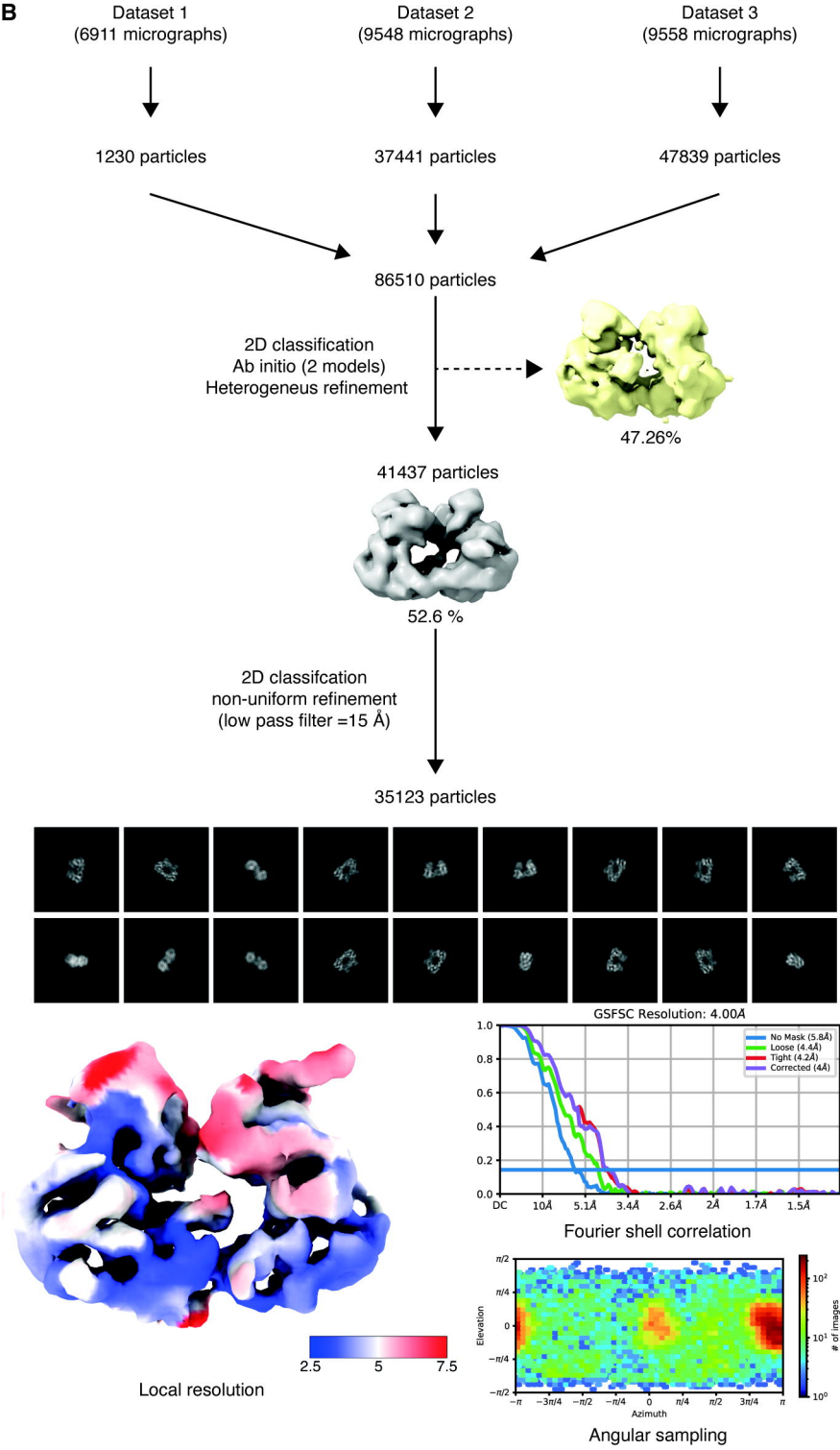
B
Dataset 1
(6911 micrographs)
Dataset 2
(9548 micrographs)
Dataset 3
(9558 micrographs)
1230 particles
37441 particles
47839 particles
86510 particles
2D classification
Ab initio (2 models)
Heterogeneus refinement
47.26%
41437 particles
52.6 %
2D classifcation
non-uniform refinement
(low pass filter =15 Å)
35123 particles
GSFSC Resolution: 4.00Å
No Mask (5.8Å)
Loose (4.4Å)
Tight (4.2Å)
Corrected (4Å)
DC
10Å
5.1Å
3.4Å
2.6Å
2Å
1.7Å
1.5Å
Fourier shell correlation
2.5
5
7.5
Local resolution
Elevation
Azimuth
# of images
Angular sampling

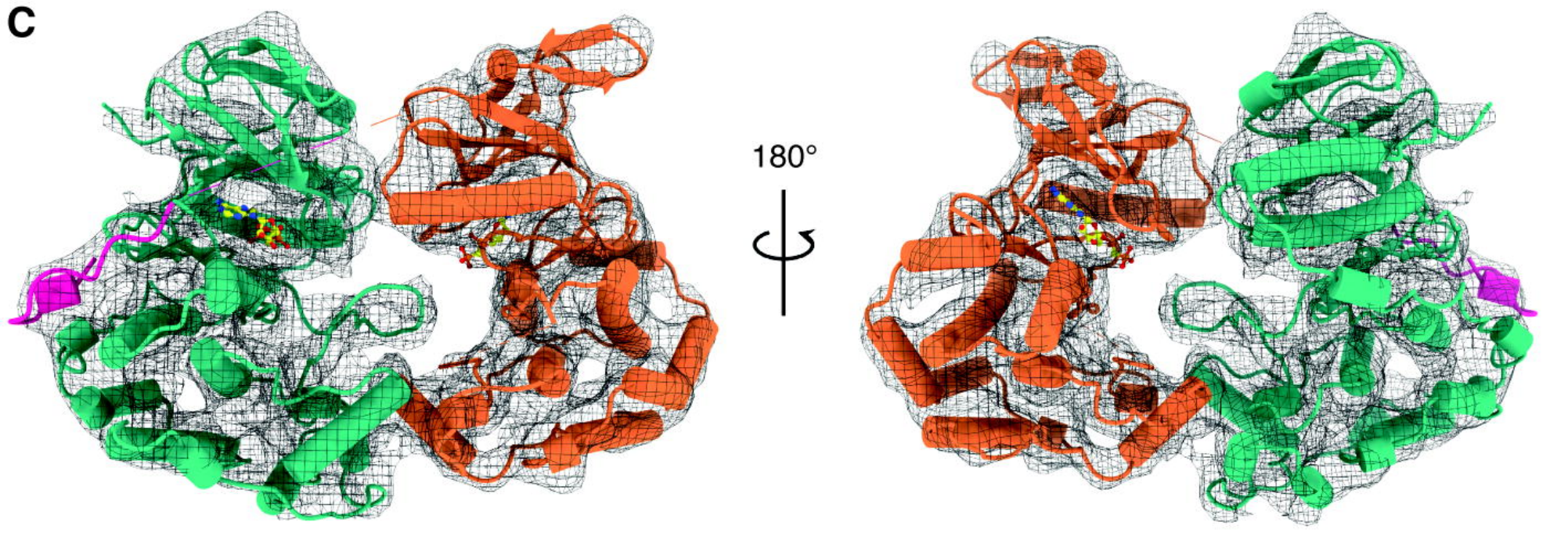
C
180°

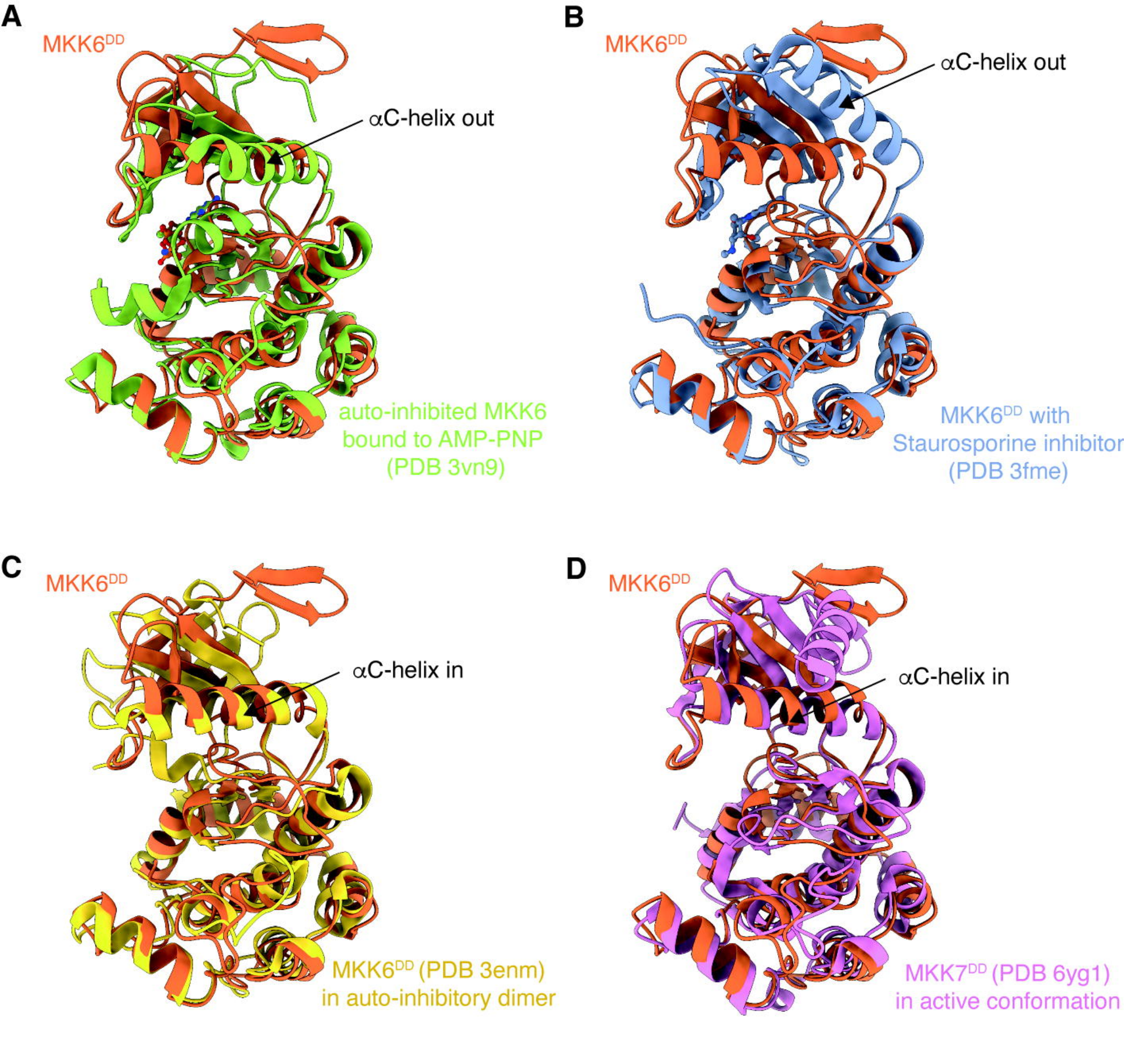
A
MKK6DD
αC-helix out
auto-inhibited MKK6
bound to AMP-PNP
(PDB 3vn9)
B
MKK6DD
αC-helix out
MKK6DD with
Staurosporine inhibitor
(PDB 3fme)
C
MKK6DD
αC-helix in
MKK6DD (PDB 3enm)
in auto-inhibitory dimer
D
MKK6DD
αC-helix in
MKK7DD (PDB 6yg1)
in active conformation

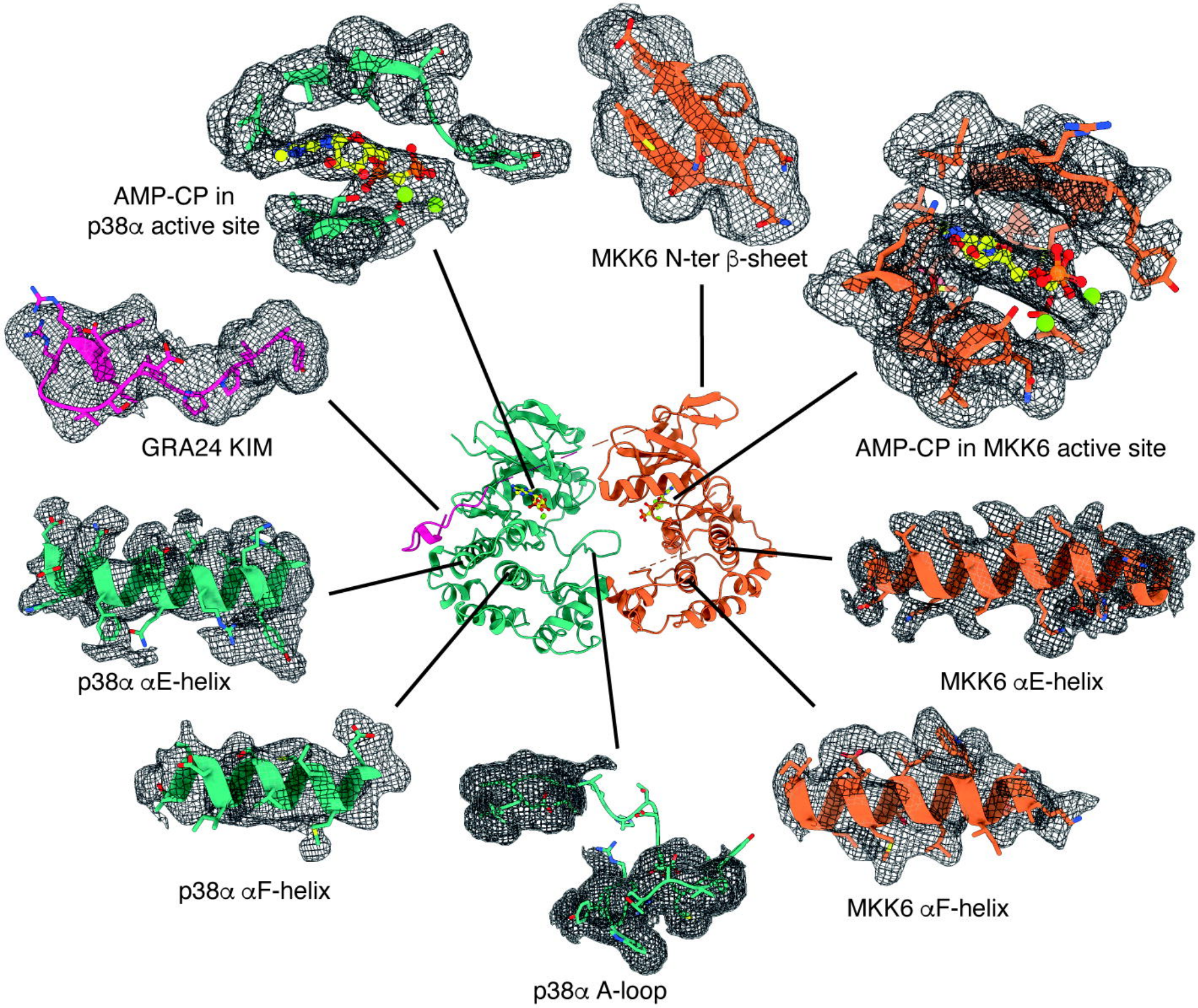
AMP-CP in
p38α active site
MKK6 N-ter β-sheet
GRA24 KIM
AMP-CP in MKK6 active site
p38α αE-helix
MKK6 αE-helix
p38α αF-helix
MKK6 αF-helix
p38α A-loop

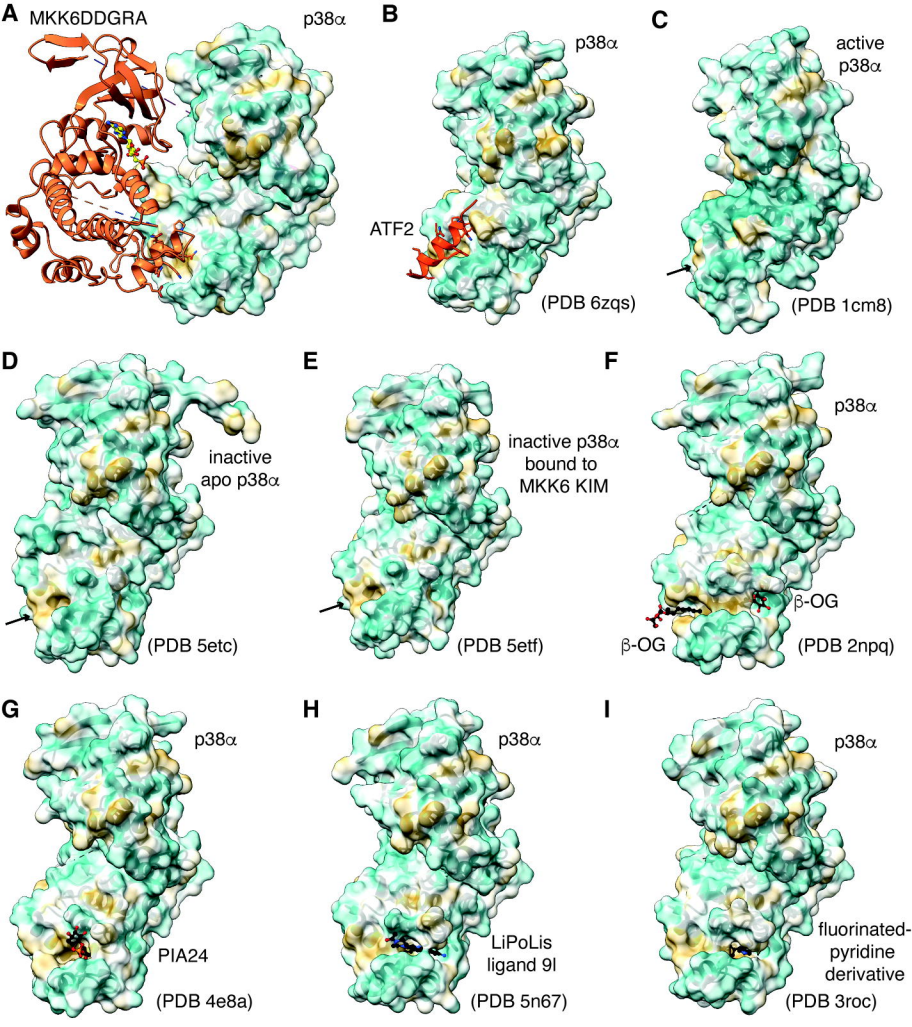
A
MKK6DDGRA
p38α
B
p38α
ATF2
(PDB 6zqs)
C
active
p38α
(PDB 1cm8)
D
inactive
apo p38α
(PDB 5etc)
E
inactive p38α
bound to
MKK6 KIM
(PDB 5etf)
F
p38α
β-OG
β-OG
(PDB 2npq)
G
p38α
PIA24
(PDB 4e8a)
H
p38α
LiPoLis
ligand 9l
(PDB 5n67)
I
p38α
fluorinated-
pyridine
derivative
(PDB 3roc)

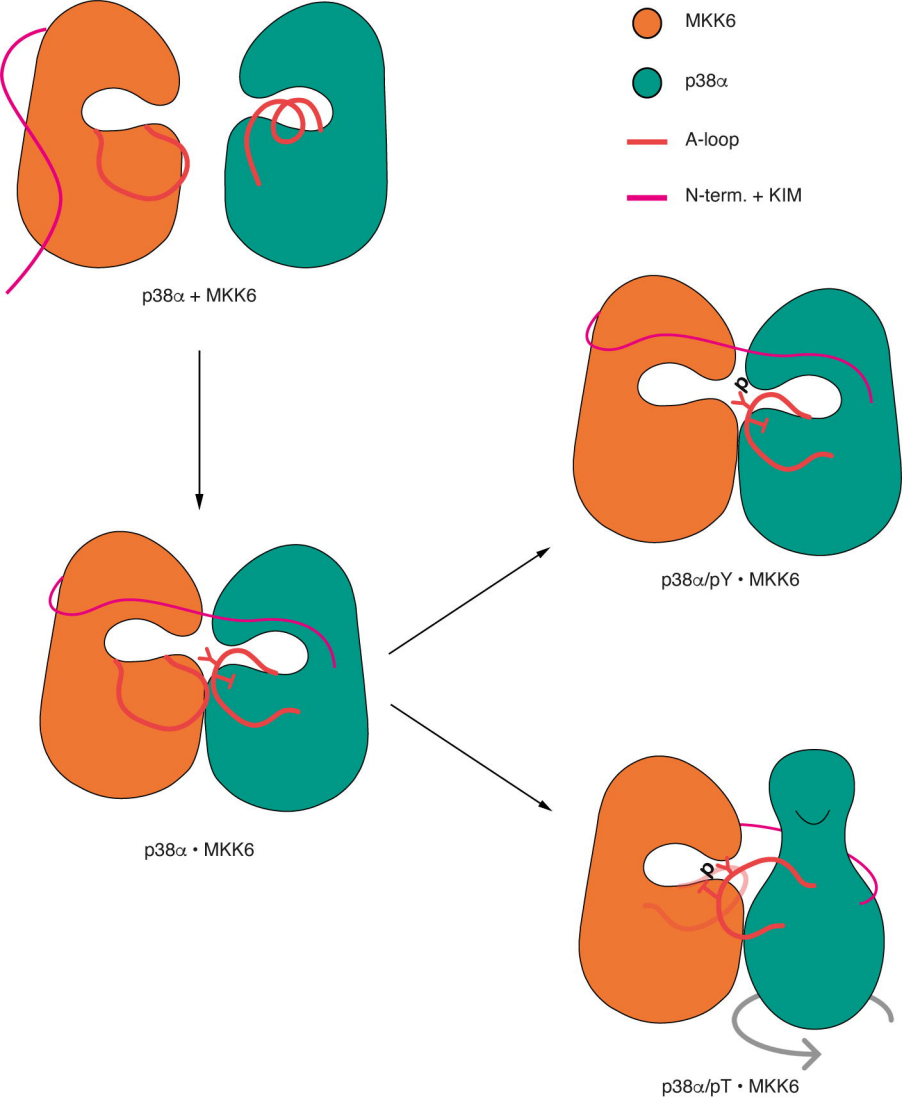
MKK6
p38α
A-loop
N-term. + KIM
p38α + MKK6
p38α • MKK6
p38α/pY • MKK6
p38α/pT • MKK6

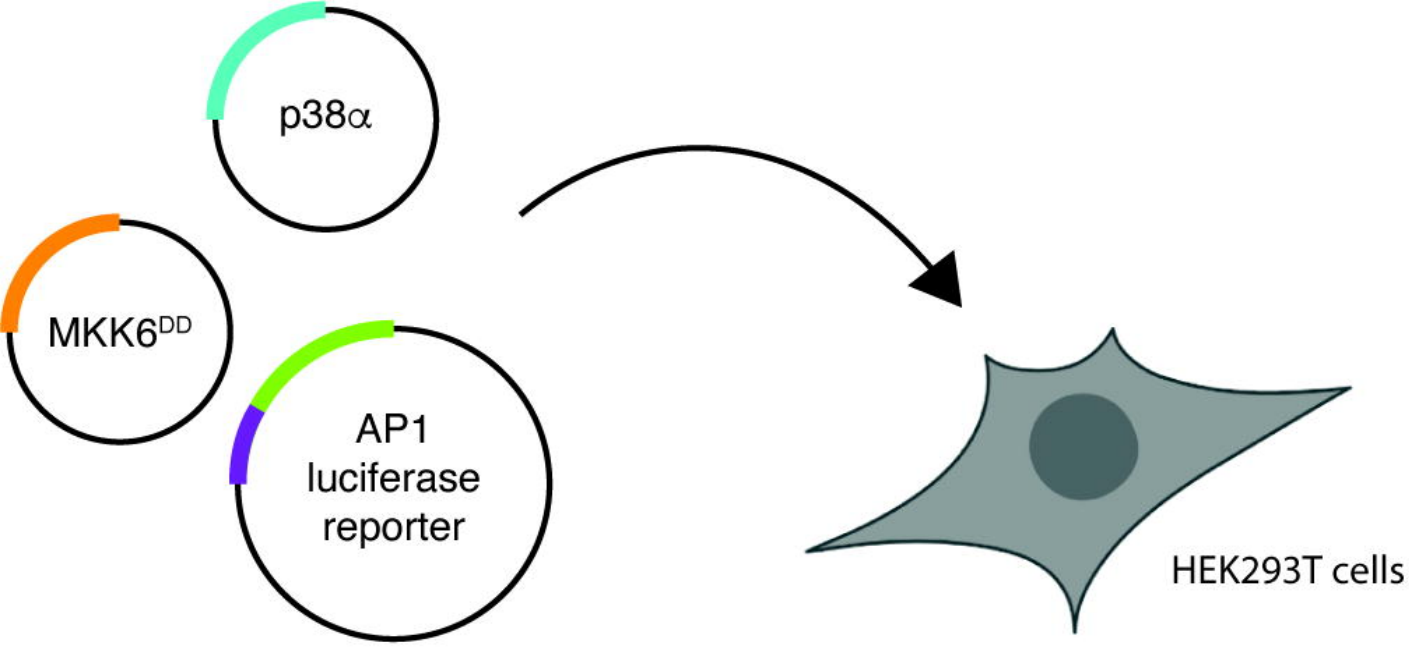
p38α
MKK6DD
AP1
luciferase
reporter
HEK293T cells

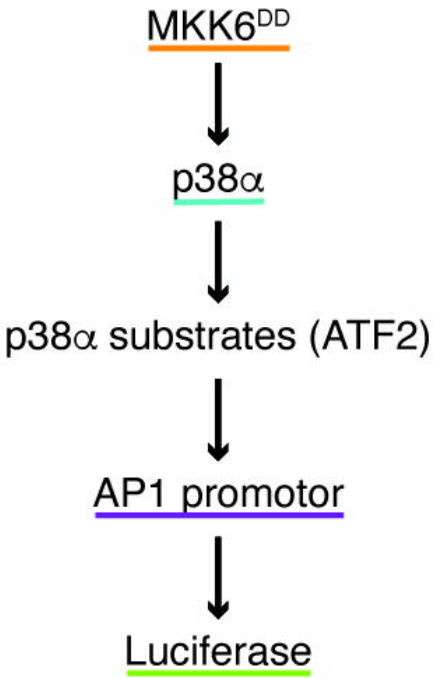
MKK6DD
p38α
p38α substrates (ATF2)
AP1 promotor
Luciferase

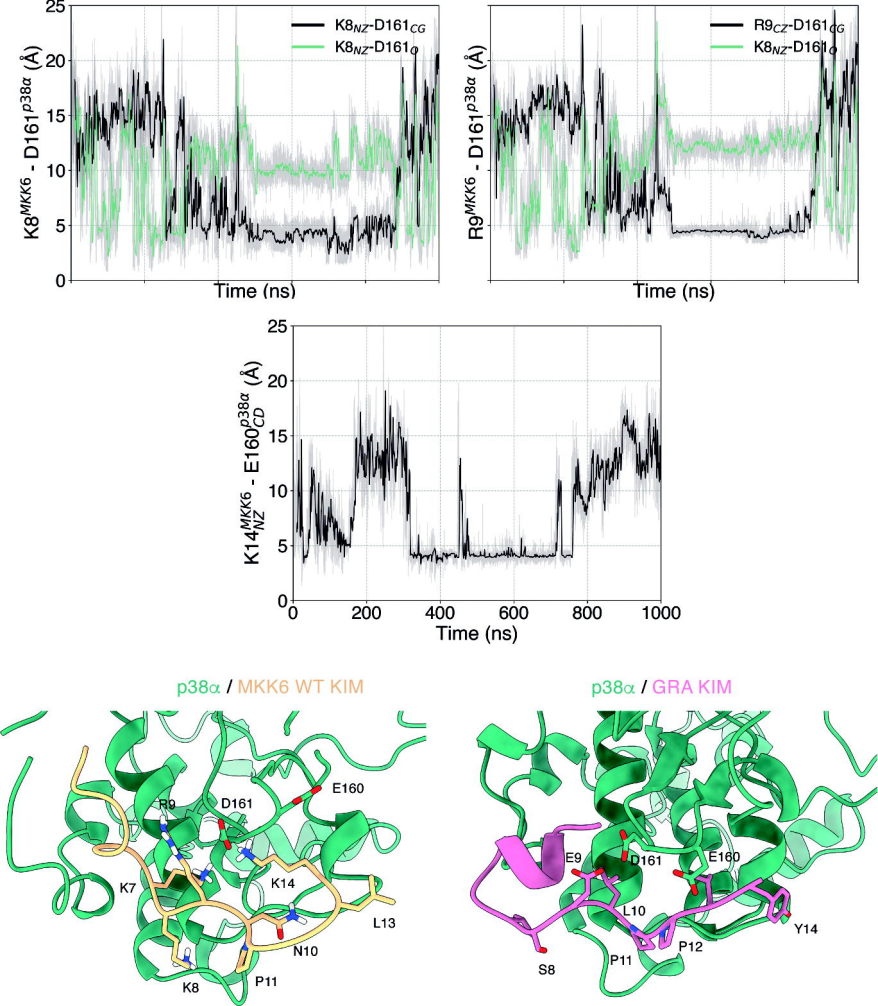
K8NZ-D161CG
K8NZ-D161O
K8MKK6 - D161p38α (Å)
Time (ns)
R9CZ-D161CG
R9MKK6 - D161p38α (Å)
K14NZMKK6 - E160CDp38α (Å)
p38α / MKK6 WT KIM
R9
D161
E160
K7
K14
L13
N10
K8
P11
p38α / GRA KIM
E9
D161
E160
L10
Y14
P12
P11
S8